

THESIS

TIDALLY INDUCED SEISMICITY AT THE GROUNDED MARGINS OF THE ROSS ICE  
SHELF, ANTARCTICA

Submitted by

Hank M. Cole

Department of Geosciences

In partial fulfillment of the requirements

For the Degree of Master of Science

Colorado State University

Fort Collins, Colorado

Summer 2020

Master's Committee:

Advisor: Richard C. Aster

Daniel McGrath

Margaret Cheney

Harley Benz

Copyright by Hank M. Cole 2020

All Rights Reserved

## ABSTRACT

### TIDALLY INDUCED SEISMICITY AT THE GROUNDED MARGINS OF THE ROSS ICE SHELF, ANTARCTICA

Repeating swarms of local icequakes were recorded by broadband seismographs deployed near the grounding line of the Ross Ice Shelf, Antarctica from late 2014 to early 2017. Swarms commonly persist for over six hours and contain thousands of events. Most swarms are induced or enhanced by tidal forcing. The number of events and event amplitudes in a swarm is most correlated with the modeled tide range. Some swarms only occur during cold periods of the austral winter. Icequakes are cataloged using a cross-correlation detector after building a template library from clustered STA/LTA picks and epicenters are estimated for high quality events. Events can be classified into four broad categories. The first event type is the most common (>95% of events) and occurs in diurnal swarms at all times of year. This type of event is interpreted to be sourced by propagation of near surface crevasses due to enhanced tensile stress from downward flexure of the ice shelf during falling tide. The second type of event has similar waveforms but occurs at the crest of large spring tides and appears to have an englacial or basal source. The third type of event is likely sourced from within the firm, possibly related to densification. It is also observed at stations in the ice shelf interior, but appears enhanced by tides at stations near the grounding line. The fourth type of event is only observed at a station on the Steershead Ice Rise. These are sweeping harmonic tremors lasting up to 8 s that start at low frequency and then tail upwards into an impulse like signal. This work characterizes these icequake types and their correlation to tidal and environmental forcing. It also details a single station event location scheme that is to used to further interpret events by finding their back azimuth with a polarization analysis and estimate their source-receiver distance with two methods. These observations provide insight into the deformation and brittle fracture at the grounded margins of the Ross Ice Shelf.

## ACKNOWLEDGEMENTS

I would like to thank my Advisor Rick Aster for his support and sage advice while conducting this research. My thanks also go out to committee members Margaret Cheney, Dan McGrath, and Harley Benz for agreeing to critically review this work. Dr. Michael Baker, Julien Chaput, and David Heath were also extremely helpful in troubleshoot technical issues. My other fellow CSU graduate students deserve praise for providing an encouraging community. I would also like to thank the National Science Foundation for funding this work and also CSU donors that contributed to the McCallum Scholarship which provided additional assistance while completing this work. Finally I would like to thank my wife for her patience while I was busy with this research.

This work was supported by U.S. National Science Foundation grants 1744852, and 1141916, and all seismic data utilized in this study can be obtained from the IRIS Data Management Center ([www.iris.edu](http://www.iris.edu)). Thanks go to the many people involved in the successful deployment of the ANET and RIS/DRIS seismic stations as well as Raytheon Polar Services, Antarctic Support Contract, the New York Air National Guard, and Ken Borek Air for logistical support. Thanks also go to the IRIS-PASSCAL Instrument Center for polar instrumentation and field support. IRIS is funded through the Seismological Facilities for the Advancement of Geoscience (SAGE) Award of the National Science Foundation under Cooperative Support Agreement EAR-1851048.

## TABLE OF CONTENTS

ABSTRACT . . . . .	ii
ACKNOWLEDGEMENTS . . . . .	iii
LIST OF FIGURES . . . . .	vi
Chapter 1      Background . . . . .	2
1.1          Geologic Setting . . . . .	2
1.2          Ice Shelf Features . . . . .	3
1.2.1      Ice Shelves . . . . .	3
1.2.2      The Grounding Line . . . . .	4
1.2.3      Crevasses . . . . .	5
1.2.4      Firn . . . . .	6
1.2.5      The Buttressing Effect . . . . .	6
1.2.6      Ice Shelf Seismicity . . . . .	7
Chapter 2      Research Methodology . . . . .	9
2.1          Data . . . . .	9
2.1.1      Seismic Data . . . . .	9
2.1.2      Tidal Data . . . . .	11
2.1.3      Environmental Data . . . . .	13
2.1.4      Remote Sensing . . . . .	14
2.2          Event Detection . . . . .	14
2.2.1      Basic Signal Analysis . . . . .	15
2.2.2      REDPy and STA/LTA detection . . . . .	16
2.2.3      Event Templates . . . . .	19
2.2.4      Cross-Correlation Detection . . . . .	20
2.2.5      Swarm Aggregation . . . . .	21
2.3          Locating Events . . . . .	22
2.3.1      Polarization Analysis . . . . .	22
2.3.2      Ranging by Arrival Time Difference . . . . .	24
2.3.3      Ranging by Modeling Dispersion . . . . .	25
2.4          Icequake Swarm Classification . . . . .	29
2.4.1      Type A: Falling Tide . . . . .	31
2.4.2      Type B: High Stand . . . . .	32
2.4.3      Type C: Cold Snap . . . . .	36
2.4.4      Type D: Tremor . . . . .	38
Chapter 3      Tidally Induced Icequake Swarms . . . . .	39
3.1          Abstract . . . . .	39
3.2          Introduction . . . . .	40
3.3          Data . . . . .	41
3.3.1      Seismic Data . . . . .	41

3.3.2	Tidal Data . . . . .	43
3.3.3	Environmental Data . . . . .	43
3.4	Methods . . . . .	44
3.4.1	Signal Analysis and Event Detection . . . . .	44
3.4.2	Estimating Event Locations . . . . .	46
3.5	Results and Discussion . . . . .	47
3.5.1	Repeating Icequake Events . . . . .	47
3.5.2	Tidal Forcing of Icequakes . . . . .	48
3.5.3	Interpreting Icequake Types . . . . .	49
3.6	Summary . . . . .	50
Chapter 4	Discussion, Conclusions, and Future Work . . . . .	54
4.1	Event Detection Performance . . . . .	54
4.2	Tidally Induced Seismicity . . . . .	55
4.3	Event Locations . . . . .	56
4.4	Event Populations . . . . .	60
4.5	Future Directions . . . . .	63
4.6	November 26 2014 Bolide Explosion . . . . .	64
4.7	Summary and Conclusions . . . . .	65
Chapter 5	Swarmy: Automatic Analysis of Swarm Seismicity . . . . .	68
5.1	Preparing the Swarmy Environment . . . . .	68
5.2	Configuring Swarmy . . . . .	70
5.3	Running Swarmy . . . . .	73
5.4	Examining Swarmy Results . . . . .	74

## LIST OF FIGURES

2.1	The XH network deployed by the RIS/DRIS experiment. Green triangles signify stations where grounding zone seismicity is prevalent. AWS stations Margaret and Gill are marked in orange. . . . .	10
2.2	A photo of station RS08 at the end of its deployment. . . . .	10
2.3	Synthetic tides illustrating the degree of variability between stations during the same window. . . . .	12
2.4	Two years (2015 and 2016) of air temperature, relative humidity, and wind velocity at AWS Margaret after applying a 7-day lowpass filter. Missing values from instrumentation issues are linearly interpolated here but raw data used in analysis is left uninterpolated. Limits are scaled to highlight how air temperature and relative humidity vary together during the dark winter months. . . . .	13
2.5	Images from the WorldView-2 satellite showing two scales of crevasse features seen near station RS09. The left image shows surface crevasses superimposed on a depression in the ice that is consistent with thinning at the grounding line. The image on the right shows a field of mode-I dominant surface crevasses $\sim 5$ km from RS09. . . . .	15
2.6	Example event from a typical falling tide swarm recorded at RS09 that shows separation between the Love and Rayleigh phases. Seismogram was bandpass filtered 4-10 Hz, then synthetically rotated from ZNE to ZRT coordinates after determining the back azimuth from polarity/variance tensor analysis. Colors shown in the seismogram correspond to the colors in the particle motion plots. . . . .	17
2.7	Seismogram (Top) bandpass filtered 5-30 Hz showing trigger detections over one week of falling tide swarms at station RS09 and the associated STA/LTA ratio (Bottom) with activation threshold (red) and deactivation threshold (blue). Plots like these were used to evaluate the chosen STA/LTA parameters for initial icequake detection. . . . .	19
2.8	Example template from RS09 of a cluster with members from a falling tide event. Envelopes for the surface wave band (5-15 Hz) and body wave band (20-30 Hz) are shown in gold and green respectively and vertical lines denote the peak in both. . . . .	20
2.9	Resulting integration kernel contours produced by OASES-OASP for the RS09 velocity model. The red line is the 4th order polynomial fit of the fundamental mode that was derived to produce the frequency-slowness curve for group velocity. . . . .	27
2.10	Group velocity as a function of frequency in Hz for the RS09 velocity model. The subtle departures from a linear trend propagate to more curvature changes with increasing distance. . . . .	28
2.11	Example event showing the power spectrum spectrogram (top) with the best fit dispersion trace (solid red) along with two dispersion traces for other ranges (dashed and dotted red). The PSD spectrogram demeaned by frequency bin (center) shows more detail in the signal. . . . .	30
2.12	Examples of the four types of events from the located event catalog. Spectrograms are acceleration power spectral density plots demeaned at each frequency bin to improve clarity. Seismograms are rotated to ZRT domain, bandpass filtered 5-35 Hz, and scaled to have equal vertical limits for each channel. . . . .	31

2.13	Plots of 7 days of seismicity to highlight the four types of events. The top plot is a vertical velocity seismogram bandpass filtered 3-35 Hz with all figures having equal scaling. The spectrogram is a PSD demeaned at each frequency bin. Cross-correlation picks are shown in 1 hour bins along with modeled tidal range. Red boxes highlight other swarm types apart from type A. . . . .	33
2.14	Scatter plots showing correlation of tidal range, tidal rate of change, air temperature, and wind speed at stations of interest. R-squared values for linear regressions of each plot are shown. . . . .	34
2.15	Histogram of cross-correlation pick counts binned by timing relative to tidal phase. . .	35
2.16	2D histogram of cross-correlation picks at RS11 showing the type A events centered $\sim 3\pi/2$ and the type C events dispersed when temperatures are below $-30^\circ$ C. The slight preference for type C events can be seen near 0 and $2\pi$ . . . . .	37
2.17	Plot air temperature and cross-correlation pick counts binned by day showing spikes in seismicity (mostly type C) during the second winter of the RIS/DRIS deployment. .	38
3.1	Map of ice surface slope derived from Bedmap2 and XH network stations. Seismic stations are shown as white triangles. Stations of interest for this study are labeled. The mapped grounding line is shown in white. . . . .	42
3.2	Examples of the four types of events from the located event catalog. Spectrograms are acceleration power spectral density plots demeaned at each frequency bin to improve clarity. Seismograms are rotated to ZRT domain, bandpass filtered 5-35 Hz, and scaled to have equal vertical limits for each channel. . . . .	45
3.3	Example events from station RS09. The power spectral density plot (top) shows the signatures of the body waves (25-35 Hz) and surface waves (5-15 Hz) present in the seismogram (bottom). Surface wave dispersion from Rayleigh and water cavity effects are clearly visible. This plot shows average event density during a falling tide swarm with $\sim 10$ events happening every minute. . . . .	45
3.4	All tidal cycles and event counts relative to tidal phase at RS09 from 2015-2017. . . .	49
3.5	Density plot showing that separate populations of seismicity at RS11 depend on temperature thresholds and tidal forcing. . . . .	51
3.6	Timeseries of air temperature measured at AWS station Margaret and daily counts of correlation picks. . . . .	51
4.1	Cross-correlation picks relative to timing in the tidal cycle. . . . .	57
4.2	Scatter plots showing correlation of tidal range, tidal rate of change, air temperature, and wind speed at stations of interest. R-squared values for linear regressions of each plot are shown. . . . .	58
4.3	Histograms of back azimuth for located events. Events with erroneous negative arrival time difference were removed because they are more prone to poor automatic surface wave window selection and thus poor polarization analysis results. . . . .	61
4.4	Histograms of the source-receiver distance averaged between the arrival time difference dispersion ranging methods. Events with bad phase arrival time picks were not assigned a distance and therefore not included here. The effect from bunching of errant dispersion ranges can be seen in small picks at the maximum distance of the distribution in some stations (RS08, RS11, RS17) . . . . .	62

4.5 Record section of data from RIS/DRIS showing the arrival of coupled energy from the bolide airblast. The red line denotes the predicted arrival based on the speed of sound in cold air. . . . . 66

# Introduction

This thesis concerns ocean tide-induced seismicity observed on the Ross Ice Shelf (RIS), Antarctica. Spanning 500,809 km<sup>2</sup>, the RIS is the world's largest and constitutes 32% of the total ice shelf area around Antarctica (Rignot et al., 2013). It consists of structural provinces distinguished by distinct glacial fabrics resulting from varying flow rates as ice streams feeding into the RIS merge and shear (LeDoux et al., 2017). Recent seismic observations on the RIS have recorded various seismogenic phenomena including iceberg calving (Chen et al., 2019), mid-shelf rifting (Olinger et al., 2019), teleseismic excitation of plate waves (Chen et al., 2018), firm resonances (Chaput et al., 2018), wavefield coupling with sea ice (Baker et al., 2019), shockwaves from a bolide explosion, and even the recording of blue whale songs. Ice shelves are important targets of scientific study. An especially notable issue is that, because of their so-called buttressing effect, ice shelves slow the advance of land-based glacial ice into the ocean and therefore delay catastrophic global mean sea level rise and the resulting damage to society. (Paolo et al., 2015; Furst et al., 2016; Robel et al., 2017). Here, I summarize new observations of tidally forced icequake swarms that are interpreted to originate mainly from surface crevasse activity at the grounded margins of the RIS. These swarms were recorded during the approximately two-year deployment (late 2014 to early 2017) of the shelf-spanning RIS/DRIS broadband seismographic network. The findings show that swarm character is primarily governed by the size and rate of tidal cycles. This phenomenon provides a passive benchmark for monitoring fracture or other impulsive dynamic activity at grounded margins as it may evolve over time and in response to climate change. While the primary focus of this research is to document the phenomenology of seismic activity at the grounded margins of the RIS, other parallel topics were explored and are presented here as well. This text is divided into five chapters covering the background, methods, condensed publication, discussion, and a software guide respectively. Material in chapter 3 will be prepared and submitted to the American Geophysical Union's journal Geophysical Research Letters.

# Chapter 1

## Background

This chapter presents relevant information so that a reader with basic experience in Earth sciences can understand the context of this project and the significance of its findings. It includes a summary of the geologic history of the RIS, basic glaciological information relevant to the study, and basic seismological methods used in the analysis.

### 1.1 Geologic Setting

The origin of Antarctica and its modern ice sheets lies in the breakup of the supercontinent Gondwana beginning  $\sim 180$  Ma (Du Toit, 1937). The primal landmass was positioned in the far southern hemisphere, so Antarctica has remained mostly stationary over the last  $\sim 100$  Ma while the other continents drifted into their present-day arrangement. During and after the breakup of Gondwana, a long-lived subduction zone along western South America, the Antarctic Peninsula, and Marie Byrd Land dominated the tectonic regime while consuming the oceanic Phoenix Plate, of which the only remaining fragment sits at the western margin of the modern Scotia Plate. This extended subduction formed many West Antarctic geological features that exist today. The final stage of the rifting of Gondwana propagated west and initiated a short-lived period of seafloor spreading in the Weddell Sea (Cunningham et al., 1995; Maldonado et al., 2000). The onset of large-scale glaciation in Antarctica began  $\sim 32$  Ma when plate tectonics opened the Drake Passage between the southern tip of South America and the Antarctic Peninsula, which allowed for the formation of circumpolar currents that isolate the Antarctic climate (Zachos et al., 2001; Livermore et al., 2005). The circumpolar currents limit the degree of mixing between the Southern Ocean and the global oceans, which in turn keeps ocean water temperatures low, and cools polar air masses (Cristini et al., 2012). The West Antarctic Ice Sheet (WAIS), which the RIS is partially fed by, formed over the following  $\sim 10$  Ma and since has undergone periodic growth and retreat, including those controlled by astronomically-forced changes in Earth's obliquity (the angle of tilt of Earth's

rotational axis) which has an  $\sim 40$  ka cycle (Naish et al., 2009). The RIS likely followed this pattern and is currently in retreat since its greatest extent during the last glacial maximum  $\sim 20$  ka when the ice shelf was so thick and sea level so low that much of the present RIS region was grounded on the continental shelf (Anderson et al., 2002). The most recent large-scale retreat of the RIS likely started  $\sim 5$  ka with the dimensions we observe today being only present during the past  $\sim 1.5$  ka (Yokoyama et al., 2016). Currently, the Ross Ice Shelf (RIS) is Earth's largest floating mass of ice with an area of  $500,809 \text{ km}^2$ , making it more expansive than the state of California. The RIS is believed to be relatively stable in the modern climate, at least in part due to the presence of 15 or more mapped pinning points that restrain the flow of upstream ice mass (Tinto et al., 2019; Still et al., 2019). However, it remains susceptible to mass loss through enhanced basal melting should ocean temperatures continue to rise and circulation deliver increasingly warm water to the cavity of the shelf (Paolo et al., 2015; Stewart et al., 2019).

## **1.2 Ice Shelf Features**

### **1.2.1 Ice Shelves**

Ice shelves form when grounded glaciers flow into the ocean and persist over many years as snow accumulates on their surface in balance with mass loss from surface ablation or melting, basal melting, and iceberg calving. They can also form from thickening sea ice in conditions when mass is accumulated on the basal surface in addition to snowfall. Ice shelves are anchored to glaciers at an interface of Earth, ocean, and ice called the grounding line. The grounding line is an area where dynamic processes affect glacial ice as it transitions from the terrestrial to marine environments, often causing a great degree of modification to the glacier. Activity at the grounding line is the key focus of this work because suitably rapid processes release seismic energy into the ice which can be recorded by seismic instrumentation. In particular, the propagation of crevasses, other fracturing within the glacial ice, and mass movement along the basal surface have all been noted as seismic sources. Sources from brittle failure like crevasse propagation and fracturing are sometimes focused at the grounding line because of changes in the in the stress state and relative flow

velocities of ice. Sources from mass movement like stick-slip sliding or establishment of contact between ice and Earth occur at the grounding line because ice shelves are part of a continuum that flows both on land and in the ocean. Ice shelves can also be comprised of numerous major flow units with different velocities that causes suture zones to form which may host seismicity from strike-slip relative motion. These mechanisms can be driven or enhanced by periodic forcing from ocean tides, which is the subject of this thesis.

### **1.2.2 The Grounding Line**

The grounding line itself is a simplified concept of the broader dynamic margin between grounded and floating ice called the grounding zone where ocean tides exert flexural and other stress on glacial ice. The grounding zone begins where a terrestrial glacier begins to experience flexure and is slightly landward of the true grounding line where ice becomes separated from the Earth by ocean water. The grounding zone extends several km into the ice shelf until it no longer flexes nor moves in hydrostatic coupling with ocean tides (Fricker and Padman, 2006). Grounded zones can also exist at mid-shelf pinning points where an island might otherwise be present or where a sufficiently thick ice shelf makes contact with a bathymetric rise. The result is a bulge in the surface called an ice rise. The geometry of pinning points is a major second-order control on the rate at which ice shelves advance and strain, and are an increasingly important factor in understanding discharge budgets for buttressed ice shelves. Recent analysis has also shown that geometric and frictional properties of the seafloor at pinning points also plays a significant role in the forces applied to ice shelves (Still et al., 2019). The presence of a pinning point can change the flow regime of ice and cause thickening of upstream ice and/or introduce shearing (and thus seismic activity). Pinning points can also result in extension and thinning downstream. The lifespan a pinning point can be inferred from the degree to which it has imprinted a fabric on downstream ice. The degree of effective resistance from the presence of a pinning point is not exclusively dependent on geometry of the ice shelf or pinning point itself, but rather is a complicated system that is also influenced by the properties of the basal surface and subglacial material. Roosevelt Island,

the Crary Ice Rise, and Steershead Ice Rise are named and mapped ice rises located in the eastern half of RIS where this work is focused. Other small unnamed rise features are located in eastern RIS as well. These features act as pinning points and likely host tidally induced icequake swarms like those examined in this work. Throughout this text the grounding zone is often referred to as the grounded margin to imply a slightly larger area where seismogenic processes may occur but the ice is not undergoing strong flexure.

### **1.2.3 Crevasses**

A key feature on glaciers and ice shelves are crevasses, quasi-linear glacial fractures that are ubiquitous to glacial masses that are currently undergoing deformation or have during their history. Crevasses are of interest here because they are known to commonly be seismogenic and are thus relevant to the seismicity examined in this study (Aster and Winberry, 2017). The geometry of crevasse distribution, density, and orientation are indications of inherited fabrics and the current stress and strain state. Therefore they are useful markers for understanding the forces affecting glaciers and ice shelves. Crevasses can form at the surface or base of ice shelves from a variety of transtensional and flexural stress states. Surface crevasses are commonly seeded by fracture at depths of 15-30 m then expand upwards resulting in the characteristic surface feature (Colgan et al., 2016). Basal crevasses form in a similar way on the underside of glaciers when stress is suitably extensional and may persist if water pressure is sufficient to counteract the tendency to close or heal from the weight of the overlying ice. The presence of basal crevasses can concentrate deformation stresses conducive to the formation of surface crevasses and the two are often spatially associated (Daniel et al., 2012). Crevasses can be described by one of three fracture modes: Mode I (opening) is the result of tension, mode II (sliding) is the result of in-plane shear offset, and mode III (tearing) the result of out-of plane shearing. The reality is more complex and most crevasses are mixed-mode resulting from a combination of fracture processes. Crevasses are particularly important for studies of ice shelves, because their propagation provides a conduit for meltwater

infiltration which enhances the conditions conducive to ice shelf disintegration (Daniel et al., 2012; Scambos et al., 2000).

#### **1.2.4 Firn**

Firn is a structural feature on the surface of glaciers and ice shelves that is a nearly continuous gradient from newly accumulated snow to blue glacial ice. As snow is altered and buried, it compacts into larger ice grains over time through a process called densification. This process can take up to 1000's of years and is a function of the climate where a glacier sits, namely the seasonal temperature ranges and the rate of snow accumulation. The firn on ice shelves is typically thinner than on the continental ice sheets. On the RIS the firn is 40-60 m, while WAIS firn thickness is 60-70 m, and EAIS firn thickness is up to 130 m (van den Broeke, 2008). The thickness of the firn is defined by the close-off depth, where ice grains reach critical pressures and coalesces, trapping any remaining air as bubbles. Beneath this depth, ice is mostly homogeneous aside from trapped bubbles and any large structural features that may penetrate its mass. In glacial seismology, the firn provides unique challenges because of the extremely low values of seismic velocity in snow, the presence of air void porosity, the steep velocity gradient, and high attenuation.

#### **1.2.5 The Buttressing Effect**

Ice shelves are especially important targets for global scientific studies because their stability or instability will help govern mean sea level rise in the coming decades and centuries. If left unaddressed, sea level rise is one of the most destructive processes arising from climate change, and has the potential to cause over a trillion dollars in damage every year and displace tens of millions of climate refugees just within the United States (Hauer, 2017). Ice shelves can influence global sea level in two ways. First, the disintegration and melting of ice shelves directly contributes additional volume of water to the oceans because they are made from fresh water which is less dense than sea water and therefore displaces less seawater than it contains in bulk freshwater mass. However, this effect is minor; the contribution from all floating ice in the world (ice shelves and sea ice) would be a mere  $\sim 4$  cm (Noerdlinger and Brower, 2007). Second, the presence of ice shelves

results in a buttressing effect which slows the advance of terrestrial glaciers into the ocean limiting their contribution to sea level rise (Robel et al., 2017). Ice shelves do not need to completely disappear for the buttressing effect to be reduced, and even losing a small portion of an ice shelf can thus result in the significant acceleration of ice flux over the grounding line (Furst et al., 2016). Unlocking the full volume of polar ice sheets to melt into the ocean would produce an mean sea level rise of  $\sim 63.5$  m (Benn and Evans, 2014). This phenomenon was observed after the collapse of the Larsen B Ice Shelf when the tributary glaciers velocities increased 2-6 times and surface elevations became depressed in consequence to reduced buttressing which results in an increased rate of loss for grounded ice masses (Scambos et al., 2004; Rignot et al., 2004). Antarctica alone is expected to contribute over 1 m of sea level rise by 2100 and over 15 m by 2500 if humans do not take drastic steps to curb greenhouse gas emissions or otherwise reduce global warming (DeConto and Pollard, 2016). This all motivates climate-based studies to understand the processes affecting ice shelves.

### **1.2.6 Ice Shelf Seismicity**

Studies of glacial seismology present unique challenges because the harsh conditions require specialized equipment, they often grapple with the noisier environments compared to terrestrial settings, events may be very small, and there are often large numbers and diverse types of events. (Aster and Winberry, 2017; Anthony et al., 2014). A few passive seismic deployments have been conducted on ice shelves, with increasing coverage and quality in the last two decades. Ice shelves have been observed to host diverse source mechanisms resulting from processes within the ice, at calving fronts, on basal surfaces, from within the firn, and near grounding lines. Rift propagation is also a source of seismicity from within ice shelf interiors (Bassis et al., 2007; Heeszel et al., 2014; Olinger et al., 2019). Freeze-thaw and thermally influenced microseismicity was also recently shown to be associated with times of substantial of subsurface melting at the McMurdo Ice Shelf (MacAyeal et al., 2019). The periodic establishment of contact with bathymetric rises has also been proposed to cause seismicity at the base of the Ekstrom Ice Shelf and to result in surface

crevasse propagation on the overlying ice rumples (Osten-Woldenburg, 1990). Ice rises have been shown to host diurnal tidally-modulated surface crevasse propagation and basal activity correlated to fortnightly spring-neap tidal cycles (Lombardi et al., 2016). Long period and swell band ocean waves have been observed to enhance seismicity near the calving front of ice shelves and the abundance of sea-ice has been shown to correlate with changes in the wavefield (Bromirski and Stephen, 2012; Baker et al., 2019; Chen et al., 2019). Tidally modulated seismicity at the grounded margins has been observed in other instances (Barruol et al., 2013; Pratt et al., 2014; Hulbe et al., 2016). Thus, many other observations of seismic phenomena have been reported on ice shelves and those listed here are illustrative of the diversity of source mechanisms.

# Chapter 2

## Research Methodology

### 2.1 Data

#### 2.1.1 Seismic Data

Seismic data used in this work were acquired by the coupled *Mantle Structure and Dynamics of the Ross Sea from a Passive Seismic Deployment on the Ross Ice Shelf* (also abbreviated RIS, with stations designated RS) and *Dynamic Response of the Ross Ice Shelf to Wave-Induced Vibrations* (DRIS, with stations designated DR) projects that installed continuously recording seismographs on the ice shelf for  $\sim 2$  years between late 2014 to early 2017 (Bromirski et al., 2015)(doi:10.7914/SN/XH\_2014). Here, the acronym RIS is used only to mean the Ross Ice Shelf while RIS/DRIS is used to refer to this seismic experiment. The RIS/DRIS network (Figure 2.1) consisted of 34 broadband seismic stations adapted for polar conditions that were arranged in a transect array centered at  $78.96^{\circ}\text{S}$ ,  $179.88^{\circ}\text{W}$  with an  $\sim 1100$  km section spanning the shelf from near Ross Island to Marie Byrd Land and a  $\sim 425$  km section perpendicular to the ice front extending past the middle of the shelf. Stations were located on floating ice with the exceptions of RS08, RS09, RS11-RS14, and RS17 which were deployed on grounded ice. Floating stations were equipped with a Nanometrics Trillium 120PH posthole seismometer that was buried at shallow depth ( $\sim 2$  m) in the firn. Grounded stations were equipped with a Nanometrics Trillium 120PA seismometer that was sealed in a shallow-buried vault, with the exception of RS08 (Figure 2.2) which was a grounded station deployed with the floating instrumentation configuration. All DR stations and RS04 sampled at 200 Hz and all other (RS) stations sampled at 100 Hz. Stations were powered by solar panels and lithium thionyl chloride batteries to run continuously year-round and experienced exceptional data recovery ( $> 95\%$  at all stations). Seismic data were recorded on site and recovered by visiting and recovering stations.

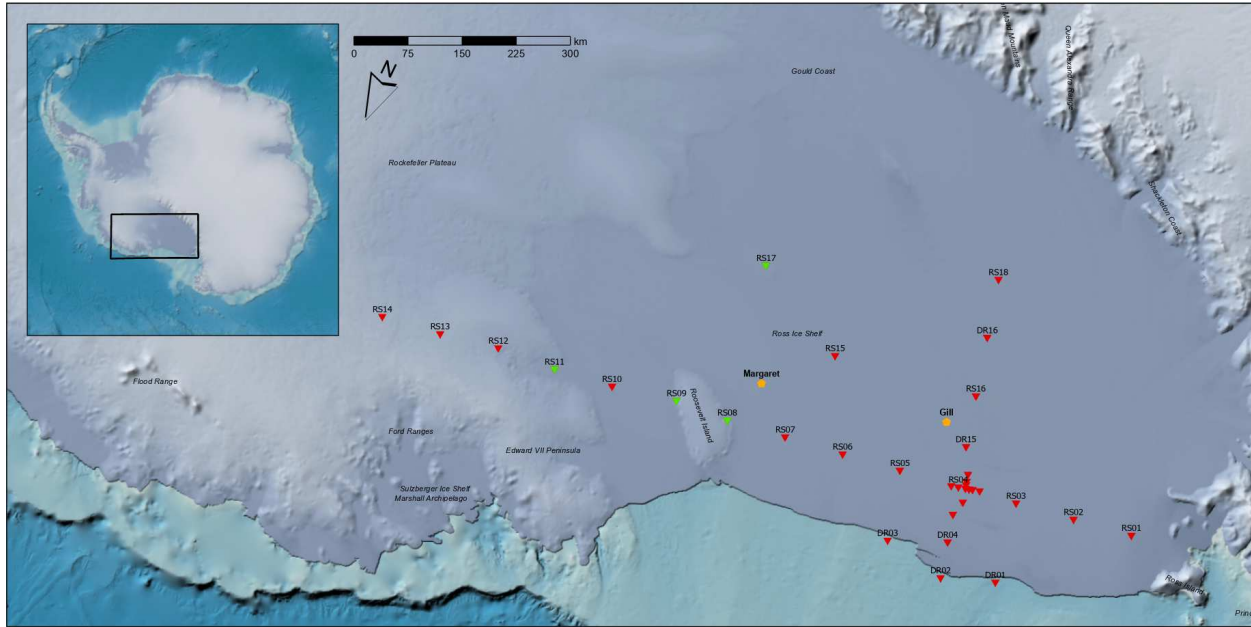


**Figure 2.1:** The XH network deployed by the RIS/DRIS experiment. Green triangles signify stations where grounding zone seismicity is prevalent. AWS stations Margaret and Gill are marked in orange.

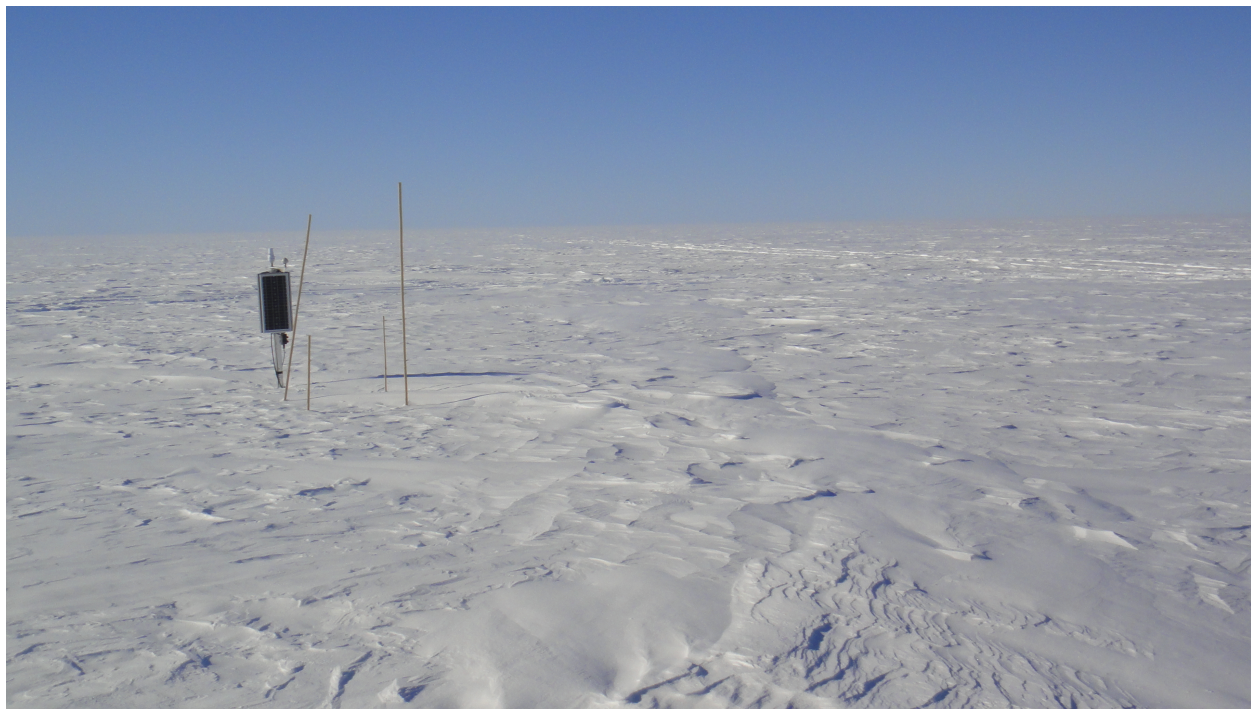


**Figure 2.2:** A photo of station RS08 at the end of its deployment.

Seismic data were accessed from the Incorporated Research Institutions for Seismology (IRIS) Data Management Center (DMC) using the web services *dataselect* function and downloaded as day-long SAC (Seismic Analysis Code) format files after requesting server-side instrument response correction and demeaning. Only 100 Hz data were used so station RS04, which would have been in the control group was not processed (DR stations were excluded due to distance from areas of interest). Processing of seismic data was done using custom software written in the Python programming language aided by the open-source ObyPy package (Krischer et al., 2015) and by extending the REDPy package (Hotovec-Ellis and Jeffries, 2016) for part of the initial event detection. See 5 for detailed information about the custom software developed for this work.

### **2.1.2 Tidal Data**

Synthetic tidal time series containing all tidal constituents resolved at 10-minute intervals were generated for each station using the Tide Model Driver (TMD) MATLAB package and an input model (CATS2008) specifically developed for tides in the Ross Sea (Padman and Erofeeva, 2005; Padman et al., 2002). For floating stations, the tide was modeled at the station location reported in metadata from the RIS/DRIS network FDSN page ([http://www.fdsn.org/networks/detail/XH\\_2014/](http://www.fdsn.org/networks/detail/XH_2014/)). Since all stations of interest where the tidally associated events are strongly observed are grounded, TMD will not produce a tidal time series for them. For these stations the model was run at the nearest valid point toward the ocean. Inland stations located in Marie Byrd (RS12-RS14) were assigned the same tidal time series as RS11 during analysis. The picked latitudes and longitudes for grounded stations are listed in table 2.1 below. It is worth noting that tides are modeled at a stationary point over the course of the RIS/DRIS experiment but in reality stations moved along with the ice shelf. However, all stations of interest are on grounded ice and moved slow enough to make this stationary point assumption reasonable. RS08, RS09, and RS17 were effectively stationary while RS11 (positioned in an ice stream) moved  $\sim 400$  m over the deployment. Additionally, while tidal time series do vary spatially over the RIS, the change at a scale of several km is small enough not to impact the results significantly.

station	latitude	longitude	distance from station (km)
RS08	-79.4121	-163.929	8.3
RS09	-79.4087	-159.646	4.5
RS11	-79.1831	-152.074	12
RS17	-81.2846	-163.235	13.7

**Table 2.1:** Nominal locations used in TMD models for grounded stations (RS12-14 are omitted).

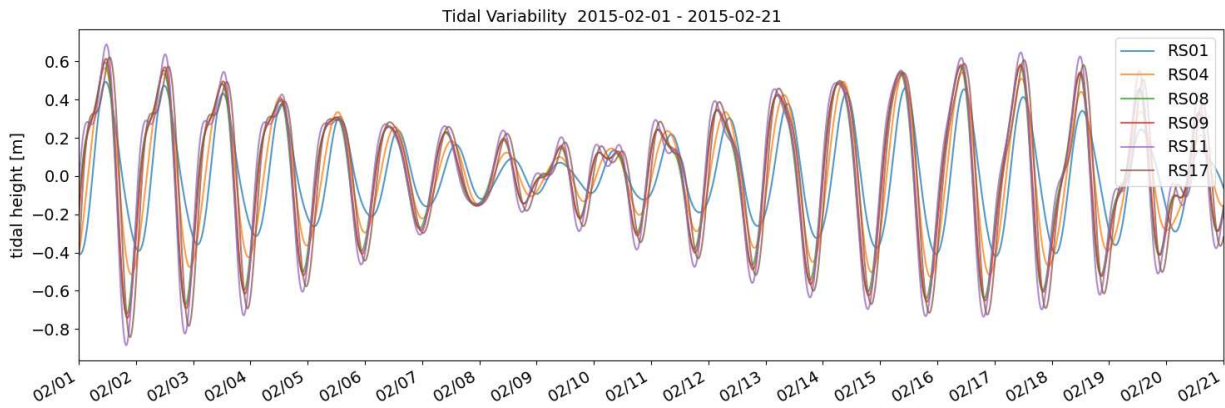


**Figure 2.3:** Synthetic tides illustrating the degree of variability between stations during the same window.

Importantly, TMD assumes a hydrostatic surface up to the grounding line and does not consider the influence of ice (Padman et al., 2003; Rignot et al., 2000). Therefore it does not account for flexure of the ice shelf at the points used, so at stations near the grounding line, tide heights overestimate the true value of displacement but are still sufficient to show tidal phases and relative forcing. The Ross Sea has a large tidal form factor, meaning the diurnal component of tides dominates unlike most other places on Earth, where the semidirunal component dominates and thus produces two high and low tides each day (Padman et al., 2018). In the Ross Embayment, typical spring tide diurnal cycles are over 1 m, while during some neap tides the range can be almost negligible for several days. As the various tidal phases migrate and stack, the length of each cycle expands and contracts so for some parts of the analysis we consider the tidal phase which is extracted from the time series by finding successive positive zero-crossings and assigning phase values for each point between.

### 2.1.3 Environmental Data

Environmental data considered in this work come from the Antarctic Automatic Weather Station (AWS) project (Lazzara et al., 2012). Observations used are 10-minute quality-controlled recordings of air temperature, atmospheric pressure, wind speed, wind direction, and relative humidity from two AWS stations (Margaret and Gill, shown on Figure 2.1). While data from both stations were used during the initial analysis of this work, only data from Margaret is presented in this thesis because it was closer to the seismic stations of interest (72 km for the closest station, RS08 and 288 km for the furthest station RS11). Data files were acquired via ftp from the archive hosted by University of Wisconsin Madison Antarctic Meteorological Research Center (<https://amrc.ssec.wisc.edu/data/>). Placeholder flag values for missing data and rare erroneous data points are removed as timeseries are called into memory for processing or plotting.

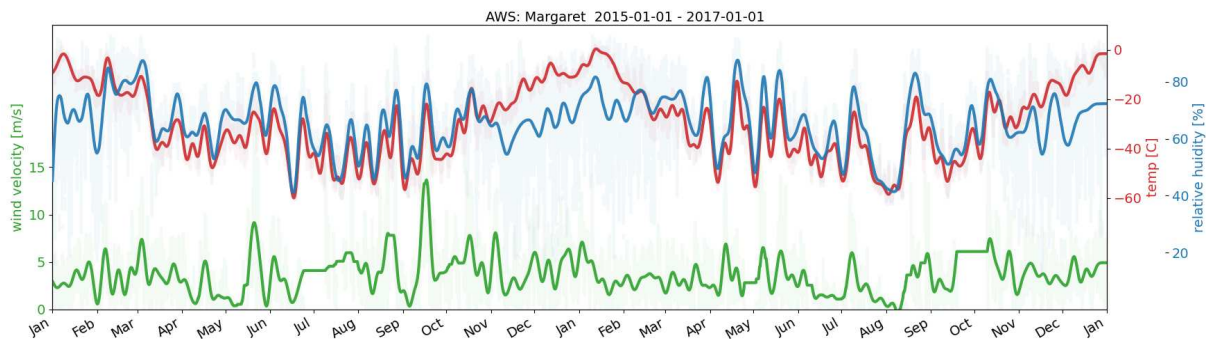


**Figure 2.4:** Two years (2015 and 2016) of air temperature, relative humidity, and wind velocity at AWS Margaret after applying a 7-day lowpass filter. Missing values from instrumentation issues are linearly interpolated here but raw data used in analysis is left uninterpolated. Limits are scaled to highlight how air temperature and relative humidity vary together during the dark winter months.

Weather data are useful for assessing if seismic sources are coupled with atmospheric drivers like temperature or wind. These data can also help interpret seismic source mechanisms in glacial environments if atmospheric conditions have an effect on seismicity. This is because because the top several meters of firn and open crevasses or rifts are susceptible to stress and other changes as thermal anomalies propagate downward. So even the absence of any correlation with environmental data can be a useful observation because it may support the interpretation of deeper source

processes. The data also prove useful for very sensitive detection schemes like that used in this work because near-surface seismometers like those in the RIS/DRIS network suffer from noise during periods of high wind where solar panels or site markers tremble and the surface topography generates high-frequency seismic signals. There are therefore times when sustained periods of high wind will render both the STA/LTA and the cross-correlation detection schemes ineffective.

Changes in temperature, insolation, firn properties, and humidity produce thermal perturbations in the thermal state of firn. These perturbations diffuse downward in the ice to depths proportional to the corresponding diffusion skin depth. Diurnal and multiday variability on the timescales of the seismic deployment are likely to only produce variations in the top meter of firn. Any correlation of icequake seismicity with short-term atmospheric changes supports interpreting a near-surface source. If variability is linked on diurnal timescales, sources are likely located close to the surface, while if variability is linked on seasonal timescales, events may be sourced deeper within the firn (up to several meters).

#### **2.1.4 Remote Sensing**

Satellite imagery was used to inspect the area surrounding some stations where icequake swarms were recorded. DigitalGlobe's WorldView satellites provide high resolution (down to 0.31 m/px) which is sufficient to distinguish significant individual crevasses or exposed glacial fabric. However, few suitable images were available over stations of interest during the deployment because of illumination angle and the lack of cloudless days, but local surface crevasse fields or shear zones are observed within 10 km at stations RS09, RS11, and RS17.

## **2.2 Event Detection**

An event detection scheme was developed to build a catalog of repeating icequakes. The process is split into two passes of the seismic data. The first pass finds short peaks in seismicity and groups these into clusters and are then used to generate characteristic templates. The second pass uses these templates to detect repeating events in swarms with a cross-correlation detector. From

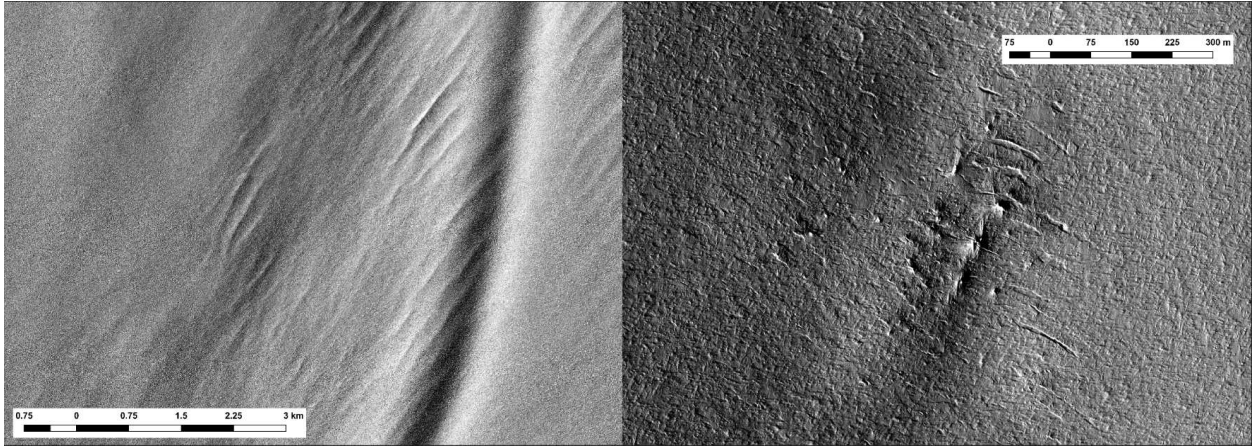


**Figure 2.5:** Images from the WorldView-2 satellite showing two scales of crevasse features seen near station RS09. The left image shows surface crevasses superimposed on a a depression in the ice that is consistent with thinning at the grounding line. The image on the right shows a field of mode-I dominant surface crevasses  $\sim 5$  km from RS09.

cross-correlation detector picks, a catalog of events is compiled and processed on a per-event basis to collect additional information from the waveforms and their associated tidal and environmental factors. Events in the catalog are then classified into types which correspond to different waveform, timing, location or other characteristics, and possible source mechanisms. These steps are detailed in the following subsections and a functional description and guide to the software written to do this is provided in chapter 5.

### 2.2.1 Basic Signal Analysis

The icequake swarms examined in this work were first identified by periodic increases of energy in month-long high frequency (1-50 Hz) spectrograms, as first noted in (Chaput et al., 2018). While similar periodic increases in energy are seen at many stations, the effect is especially pronounced at stations RS08, RS09, RS11, and RS17 which are referred to as the stations of interest in this text. The most common type of swarm occurs during falling tides, can last 3-10 hours, and can contain 1,000's of individual icequakes. These swarms have bimodal high frequency content with a strong peak centered  $\sim 8$  Hz and a subtle peak centered  $\sim 25$  Hz. Both peak frequencies vary between stations and over time. Examining individual events, we interpret the subtle peak to be body wave energy and the strong peak to be surface wave energy. The surface wave energy

is dominated by Rayleigh wave (retrograde elliptical) particle motion, but some signals show apparent Love wave particle motion after seismogram rotation to the radial-transverse domain. This is demonstrated for an example event in figure 2.6 by computing the linearity, circularity, and sphericity values for marching windows of an event (Aster et al., 1990). This shows a transition from linear (side-to-side) particle motion during the Love wave arrival, to spherical particle motion when the phases overlap, to circular particle motion (retrograde elliptical) during the Rayleigh wave arrival.

The other types of swarms have frequency content and timing relative to the tidal cycle that distinguish them from the typical falling tide icequake swarms described above. A second population of swarms occur at tidal high stands, during the highest tides of spring tide cycles. These are the most similar to the falling tide swarm, but display a higher ratio of body wave to surface wave energy. A third type of swarm that only occurs during the austral winter has events with broadly distributed frequency content with a single peak centered  $\sim 20$  Hz and no significant separation of body and surface phases. These swarms can extend for multiple days and only seem to have at best a tenuous preference for occurring during rising tides. A fourth type of swarm is exclusively observed at RS17 with the same tidal phase timing as the falling tide swarms and seems to be comprised of tremor-like events resulting from many smaller events triggering at the same location over the course of several seconds. The characteristics of each swarm type and their events are described in more detail in the section detailing icequake swarm classification below.

### **2.2.2 REDPy and STA/LTA detection**

To build event templates, the python package REDPy was used to run an STA/LTA triggering algorithm and cluster triggers based on vertical channel waveform similarity (Hotovec-Ellis and Jeffries, 2016). REDPy is an automated tool that requires no user input other than a short configuration file that defines some processing parameters. This configuration file is procedurally generated for each station by the custom wrapping software I developed (see chapter 5). While REDPy is intended to be used for cross-correlation clustering over multiple seismic stations, it is documented

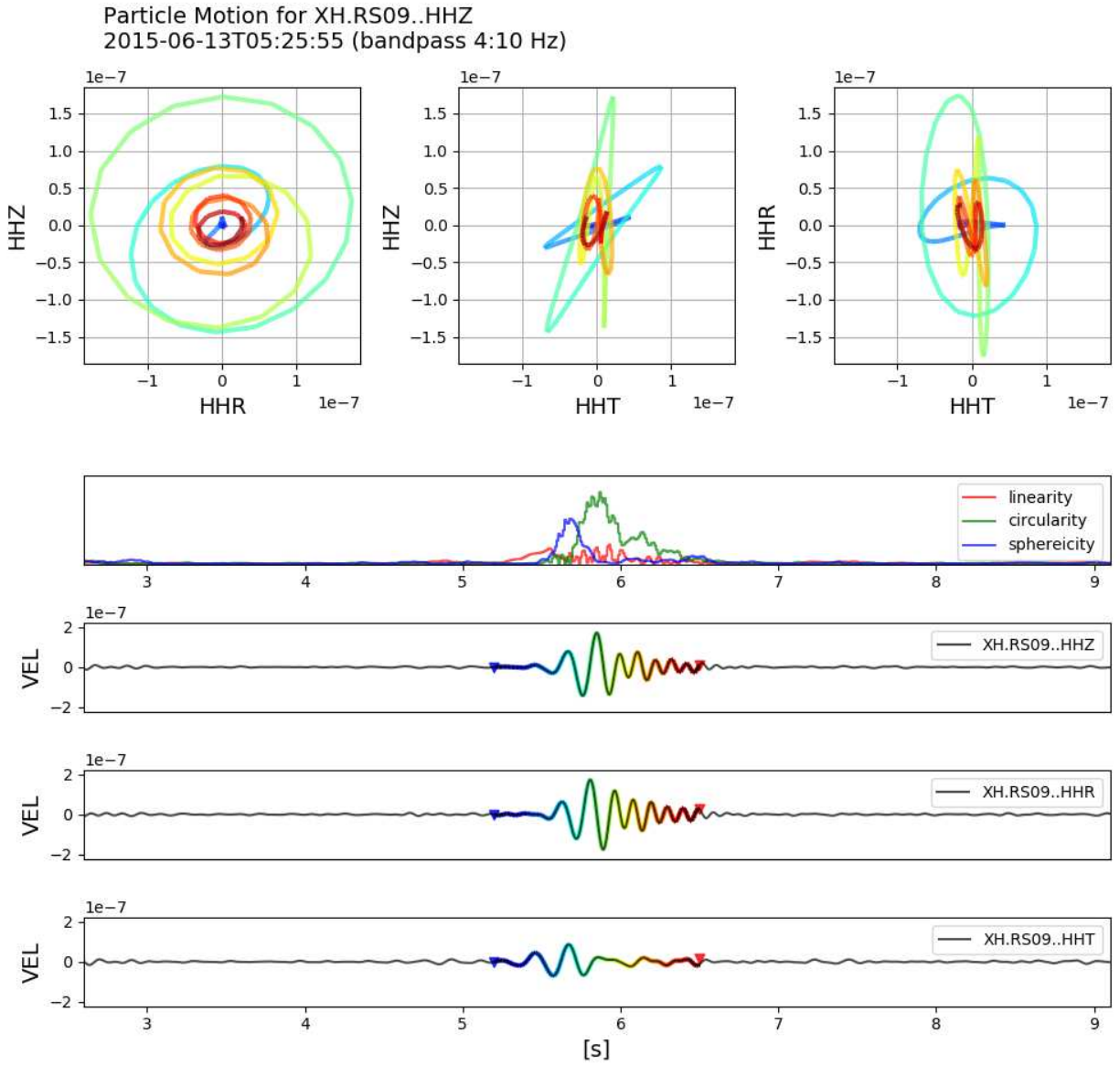


**Figure 2.6:** Example event from a typical falling tide swarm recorded at RS09 that shows separation between the Love and Rayleigh phases. Seismogram was bandpass filtered 4-10 Hz, then synthetically rotated from ZNE to ZRT coordinates after determining the back azimuth from polarity/variance tensor analysis. Colors shown in the seismogram correspond to the colors in the particle motion plots.

and tested to work well for a single station. When initially examining icequake swarms and testing software, I ran REDPy with multiple combinations of stations in the Roosevelt Island area (RS08, RS09, RS10, RS11). The output showed no repeating events that had similar character to members of icequake swarms and very few events overall, which were likely regional earthquakes or large unique icequakes. This result shows the maximum extent to which grounded margin icequake swarm energy is detectable, which must be  $<50$  km considering the average station spacing across the shelf of  $\sim 100$  km. Considering this, for each station where data is processed, REDPy is run with a single station configuration.

The two important groups of user-defined parameters in REDPy are the clustering parameters and the STA/LTA triggering parameters. For the clustering parameters, a 512 sample (5.12 s) window is used when computing cross-correlation and a similarity threshold of 0.9 is used to associate events into a cluster. If an STA/LTA detection event matches no cluster with a 0.9 similarity, it is retained in memory and attempts clustering with all following events until all data in the following 28 days has been processed and the event is labeled an orphan. The STA/LTA triggering algorithm computes the short term average (STA) of a moving window of data and the long term average (LTA) of a surrounding window, then computes their ratio as the windows advance through the data. When this ratio reaches a defined threshold the trigger is activated and when the ratio falls below the threshold, the trigger deactivates. The values used were 1.0 s for the STA window, 8.0 s for the LTA window, ratio value of 6.0 to turn the trigger on, and ratio value of 5.0 to turn the trigger off. These values were experimentally determined using the Obspy STA/LTA methods (which is the same method extended within REDPy) to ensure that most swarm events were captured and a negligible number inter-swarm events were captured. REDPy processed all available seismic data at stations of interest in the HHZ channel bandpass filtered 5-30 Hz. REDPy outputs hdf5, html, and flat text files containing its results. The html files were used to inspect results and clusters. The flat text files containing trigger times and cluster membership were used as input for creating event waveform template as described in the next subsection.

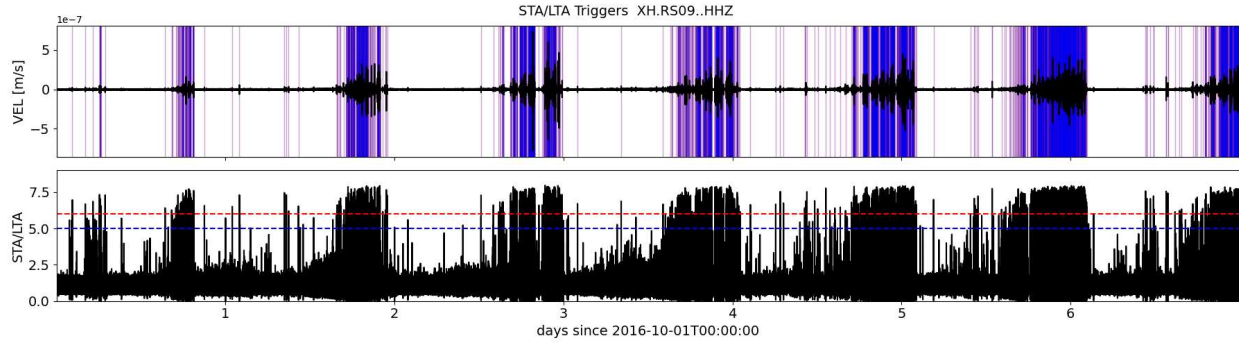


**Figure 2.7:** Seismogram (Top) bandpass filtered 5-30 Hz showing trigger detections over one week of falling tide swarms at station RS09 and the associated STA/LTA ratio (Bottom) with activation threshold (red) and deactivation threshold (blue). Plots like these were used to evaluate the chosen STA/LTA parameters for initial icequake detection.

### 2.2.3 Event Templates

From the initial catalog created by REDPy, event templates are made for each cluster. This is done by collecting the three-component waveforms for each member of a cluster, applying a bandpass filter of 5-30 Hz, then taking the mean for each channel. The waveforms do not need to be lag adjusted before taking the mean because lag was already determined during the cross correlation step in REDPy and the onset time reported in the REDPy catalog accounts for this. Each template is 10.0 seconds in length which is sufficient to capture body and surface wave arrivals together for events at all stations of interest. This window length also handles an issue where REDPy will center a detection on the body wave arrival instead of the surface wave if the ratio of body to surface wave amplitudes is sufficiently high (common for events within high stand swarms). When collecting events for a template, it is considered to be complete once 301 events have been included in the average. This is done to save on compute time as some templates would otherwise contain several 1,000s of members but have not appreciable improvement on template quality. Plots for each template are generated and the associated template waveforms are stored in pickle files (a way to export python variables held in memory in a serialized format) for ad hoc inspection and use in the correlation detection.

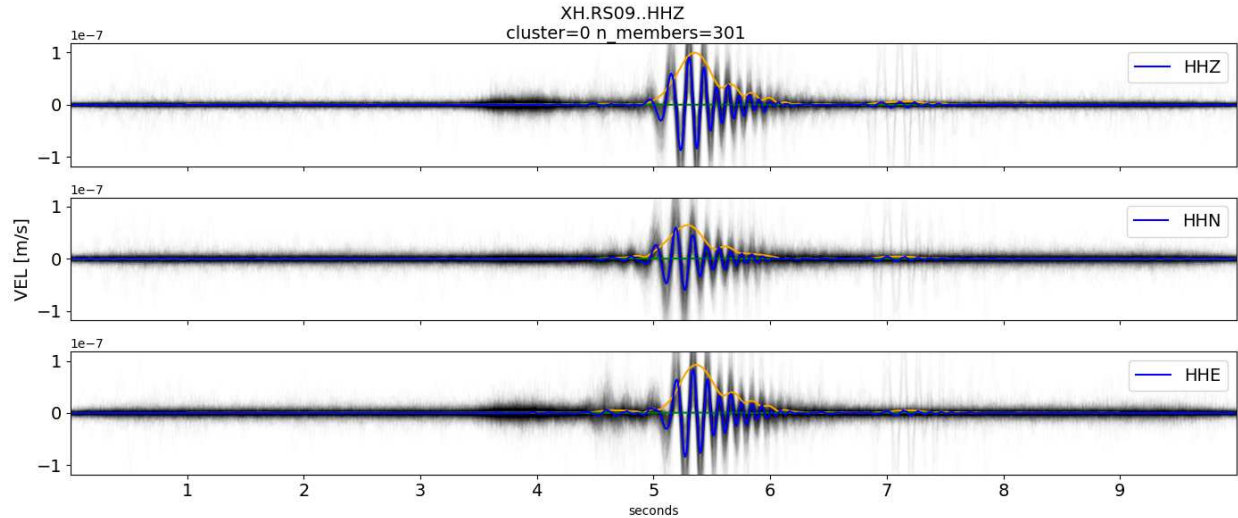


**Figure 2.8:** Example template from RS09 of a cluster with members from a falling tide event. Envelopes for the surface wave band (5-15 Hz) and body wave band (20-30 Hz) are shown in gold and green respectively and vertical lines denote the peak in both.

## 2.2.4 Cross-Correlation Detection

A cross-correlation detector takes one or more template events or a synthetic template, and passes it over marching windows of seismic data while computing the cross-correlation values at each step. When the cross correlation value reaches a user-defined threshold, a detection is extracted from the seismic data. The method is further improved by moving the template back and forth in finer resolution near the event to determine the lag from initial detection that maximizes the cross-correlation value. Using a cross-correlation detection scheme to build a catalog of events is desirable in this case because a very large number of repeating events are observed and they are often recorded in such rapid succession that methods like STA/LTA alone will miss many detections. Also, sustained periods of high wind on the RIS can introduce sufficient noise in seismic data, that while events are still recognizable, the user-selected STA/LTA parameters no longer result in an accurate count of events. Cross-correlation schemes are less affected by this because they are less sensitive to noise surrounding an event. They are also less prone to bias from selecting STA/LTA parameters which may result in varying effectiveness at different stations.

A final catalog of detections is generated using the cross-correlation detector method in the Obspy python package. The template library generated from the REDPy results is filtered to remove

templates with less than 15 members. This number was chosen from visual inspection of template plots to ensure sufficient signal-to-noise of templates. Templates are also tapered to reduce noise, and reduce effects when coda are long. The cross-correlation detector is then run over seismic data, producing a pick when at least one template reaches the similarity threshold of 0.7. When multiple templates exceed this threshold, the pick is associated with the template of highest similarity value. This was initially written to be done with three-component waveforms, but later reduced to the single vertical channel to save on compute time. Likewise, a smaller similarity threshold results in a more accurate count of picks, but also adds substantially to the compute times. When this methodology is approved by committee and peer review, processing will be run again with these more sensitive parameters. Cluster names are retained from the REDPy output so that the processing steps are more easily tracked. This means that there are some cluster numbers that do not have correlation picks because their template was excluded from the library. Correlation picks are also exported to a python pickle file.

### **2.2.5 Swarm Aggregation**

Individual icequake detections are aggregated into swarms by a series of logical rules applied to a catalog of picks. This is done to the STA/LTA triggers (repeating events and orphans) of the REDPy output and to the correlation picks to produce a catalog of swarms for each. Swarms are defined by examining the timing of events relative to their preceding and following events while tracking a flag that states whether the previous event is currently considered part of a swarm. The time between events defined to start or stop a swarm is 20 minutes. When comparing an event to the previous, if events are not grouped in a swarm yet and less than 20 minutes has passed since the last event, a new candidate swarm entry is created. The following events are tested until the first case where 20 minutes has passed and the former event is declared the last member of that swarm. If less than 15 events have occurred, the candidate swarm entry is not added to the swarm catalog. This method allows small swarms to be included and can distinguish step-like swarm behaviour during atypical tidal cycles where activity stops for a significant period of time. Swarm

information including start time, stop time, number of events, tidal information, and environmental information are exported to a csv file.

## 2.3 Locating Events

Due to the spatial extent of icequake sources, their low local magnitude, and the regional spacing of the RIS/DRIS stations, epicenters cannot be determined using standard triangulation or other methods that require multiple stations. So to estimate the location of events, a single station method is employed that uses polarization analysis to determine the back azimuth from station to source and uses two methods to estimate the source-receiver distance. The first method to estimate distance is a simple arrival time difference. The second method to estimate distance leverages the Rayleigh wave dispersion present in most icequake signals. Single station methodologies, including the one used in this work, are notoriously unreliable for producing accurate epicenters. However, with the great abundance of events in the correlation picks catalog, the distribution of back azimuth and range can provide insight to source mechanisms of icequake signals and provide first order information on the true location of sources. Locating events is computationally expensive, so only correlation picks with a similarity of greater than 0.8 are located.

### 2.3.1 Polarization Analysis

Back azimuths are estimated using a form of polarization analysis from particle motion (Vidale, 1986; Aster et al., 1990). This method uses a window of three-component time series to solve for the plane where most particle motion is occurring. If this window is limited to surface waves and it is assumed they are dominated by counter-clockwise Rayleigh motion, the result is the normal vector that describes that motion. This normal vector can then be projected onto the horizontal plane and the back azimuth can be determined. Assuming that  $\vec{X}$  is the three-component time series of the surface wave (in ENZ channel order) the variance tensor is

$$\mathbf{V} = \vec{X} \vec{X}^T, \quad (2.1)$$

where  $\vec{\mathbf{X}}^\top$  is simply the transposed three-component time series. The resulting variance tensor is a  $3 \times 3$  matrix. This is normalized by simply dividing by the trace of the tensor.

$$\hat{\mathbf{V}} = \frac{\mathbf{V}}{\text{Trace}(\mathbf{V})} \quad (2.2)$$

The result is a unit scaled tensor that characterizes an ellipsoid representing signal power in orthogonal directions with semiaxes  $\hat{e}_i$  found by solving for the eigenvectors that are scaled by  $\lambda_i$ , their respective eigenvalues. These eigenvalues and eigenvectors were solved for using the normalized variance tensor  $\hat{\mathbf{V}}$  as input to the NumPy eig function. Sorting the eigenvalues from largest to smallest allows us to reorder the respective eigenvectors by what proportion of the signal power they represent. Since we are assuming circular particle motion this should be

$$\lambda_1 \approx \lambda_2 \geq \lambda_3 \geq 0 \quad (2.3)$$

which allows us to pull values from the ordered eigenvectors that describe the normal vector to the plane of Rayleigh particle motion. Then the back azimuth is computed by projecting this vector into onto the Northing-Easting plane, adding  $90^\circ$  to make it in-line with radial particle motion, then testing the particle motion to resolve  $180^\circ$  ambiguity. This last part is done by rotating the ZNE seismogram to ZRT using the test back azimuth, then taking successive pairs of points in the vertical and radial channels to calculate counter-clockwise radial angle, which is summed over all pairs of points and scaled by the average amplitude of the pair to weight the contribution from real surface wave energy in cases with erroneously long or noisy windows. If the resulting summed angle (the value of which has no physical meaning) is negative, the  $180^\circ$  is added or subtracted to return the final back azimuth with correct Rayleigh orientation. This method assumes that we are not observing any prograde Rayleigh particle motions, which should only be observed at a depth  $\sim 20\%$  of the dominant wavelength which in the case of these events corresponds to  $\sim 30$  meter depth (Stein and Wysession, 2009).

### 2.3.2 Ranging by Arrival Time Difference

The first ranging method is a simple arrival time difference that takes automatically picked phase arrivals for the body and surface waves and uses two assumed values for their propagation velocities. This uses the equation

$$D = \frac{\Delta t}{\frac{1}{V_{Rayleigh}} - \frac{1}{V_P}} \quad (2.4)$$

where  $D$  is the distance to the event in km,  $\Delta t$  is the measured arrival time difference in seconds,  $V_P$  is the P-wave velocity, and  $V_{Rayleigh}$  is the group velocity of the Rayleigh wave train. The velocity values are assumed to be  $V_P = 3.870$  km/s and  $V_{Rayleigh} = 1.550$  km/s which are applied to all events and stations (Walter et al., 2015a; Olinger et al., 2019). Too many events exist in the catalog for manual picking of arrival times to be a reasonable task. So arrival times are automatically picked from the vertical channel for each event by bandpass filtering the signal separately to the typical body wave (25-35 Hz) and surface wave (5-15 Hz) bands then finding the first time that envelope of each band rises a certain level above a threshold. The body wave pick is meant to represent the P-wave arrival time and the surface wave pick is meant to represent the Rayleigh wave arrival time. For the both bands, the threshold is the average value of the envelope over the 10.0 seconds event window. For the body wave band, the first 1.5 seconds of the envelope are zeroed to depress the threshold and filter erroneously early picks from smaller events in the observation window. For the surface wave band, the first 2.5 seconds and last 2.5 seconds of the envelope are zeroed out to depress the threshold and limit the number of cases where multiple icequakes in the event window cause erroneous picks. The surface wave window can be tighter because observation windows typically are centered on the surface wave arrival and in the cases when they are not, the body and surface wave is still caught in the smaller 5.0 second window. The body and surface wave bands trigger an arrival pick at the first instance where the envelope reaches a threshold of 2.75 and 3.0 times the mean of the modified envelopes respectively. The values of zero-trimming the the threshold were determined experimentally by inspecting the results from many events. The threshold for the surface wave band is larger because it is an emergent arrival that contains Love and Rayleigh energy, but the arrival time difference expects the later. The accuracy

of this method is limited because it assumes a direct propagation path (which is only valid for very near-surface sources), it does not account for spatial variations in propagation velocity, and it is prone to errors in arrival time picks. This method does produce reasonable results for event types A and B which comprise the majority of events. It can produce reasonable results for event type C, but a range is not computed if the body wave pick is later than the surface wave pick which can happen if these events are particularly impulse-like and causes an erroneous body wave pick to be in the surface wave coda. It also does not produce useful picks or distance estimates for the type D tremor events because their waveform contains many sub-events and does not follow the assumptions needed for this estimate. Even though distance estimates may not be accurate for event types C and D, applying the phase arrival picks provides useful derived measurements for differentiating event types because it contains information about the relative timing of energy arriving in the two frequency bands.

### **2.3.3 Ranging by Modeling Dispersion**

A second attempt at estimating the source-receiver distance for icequakes is made by leveraging the Rayleigh wave dispersion seen in nearly all events. Rayleigh waves are P and SV polarized surface waves that exist when there is a near-tractionless surface on a halfspace such as Earth's terrestrial surface or the ocean floor (Stein and Wysession, 2009). Rayleigh waves are dispersive, and thus propagate with different apparent velocities depending on their frequency. In an environment where the velocity increases with depth, like the firm, lower frequency energy (longer wavelength) energy is sensitive to greater depths and thus higher velocities. This results in lower frequency energy travelling with a faster group velocity than higher frequencies do. In seismic data this is observed as a sweeping trend towards higher frequency signal later in the arrival of dispersive phases like Rayleigh or Love waves. This effect is enhanced in mediums with particularly steep velocity gradients like the firm. The curvature of the dispersion recorded in a seismogram is a function of the velocity structure between the source and receiver and the source-receiver distance. To estimate the distance for an event in this case a velocity model is assumed and a forward model

produces the expected dispersion traces in time-frequency space for many distances. These dispersion traces are then compared to observations to find the best model, resulting in an estimated distance. Velocity models were created for each station by combining the firm model described by Diez et al. (2016) with ice thickness, cavity thickness, and bedrock topography values averaged over the four closest pixels to station location queried from Bedmap2 (Diez et al., 2016; Fretwell et al., 2013). When there is no mapped water layer at a station, a 10 m water layer is imposed because nearly all events have back azimuths pointed toward parts of the RIS that are floating and thus have a cavity along at least part of the propagation path. These models are used as input for the OASES-OASP Fortran module which models an impulse response to determine the transfer function and the wavefield (Schmidt, 2004). The modeled impulse is defined to be at 20 m depth and the modeled receiver is defined to be at 1 m depth. With the options used for this case, OASES-OASP produces an  $\omega - k$  representation of the wavefield in the form of integration kernel contours produced using a full Hankel transform integration scheme as recommended for near-field cases. The fundamental mode dispersion curve is extracted from the  $\omega - k$  plot by collecting the positions of the largest pixel values along its path and using them to produce a 4th order least-squared polynomial fit using MATLAB's polyfit function. This is limited to the surface wave band (5-15 Hz) to avoid numerical noise at low frequencies and because most observed signals show little surface wave content above 15-20 Hz. The polynomial curve allows analytical computation of the derivative, which represents group velocity ( $U = d\omega/dk$ ), without having to handle adjacent pixels that could result in infinite group velocity. The derivative is evaluated at each  $\omega$  to determine group velocity as a function of frequency in Hz. The frequency-slowness curves vary only slightly between models for different stations because these are primarily a function of the firm velocity gradient which is defined to be the same at all stations.

This group velocity dispersion relationship is then used to model the dispersion observed in time-frequency space for a suite of distances. Time-frequency curves are generated for distances from 50 m to 8.0 km at 50 m increments. The 8.0 km limit was chosen based on results from the arrival time difference method. Also, past 8.0 km the dispersion at high frequencies would be so

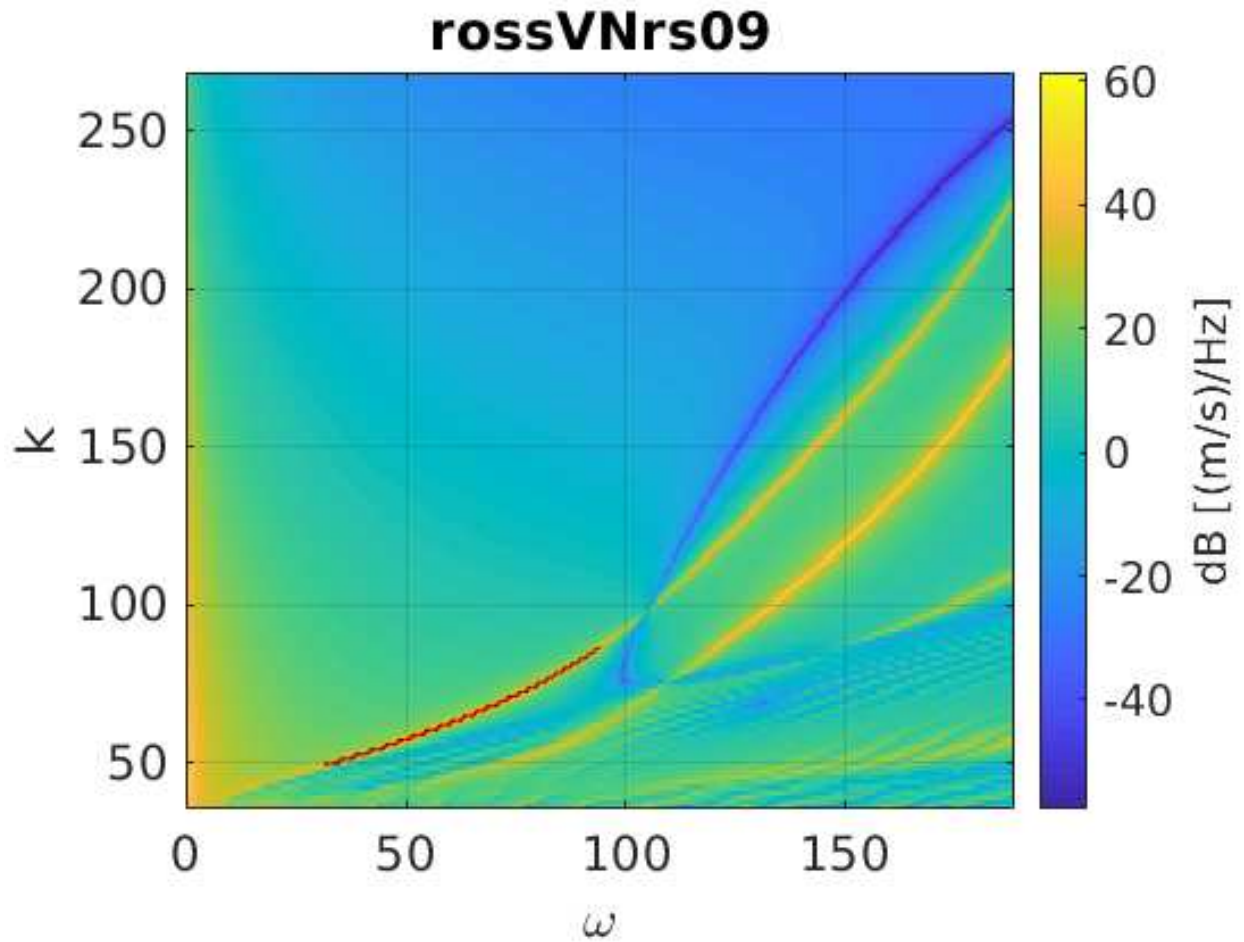


**Figure 2.9:** Resulting integration kernel contours produced by OASES-OASP for the RS09 velocity model. The red line is the 4th order polynomial fit of the fundamental mode that was derived to produce the frequency-slowness curve for group velocity.

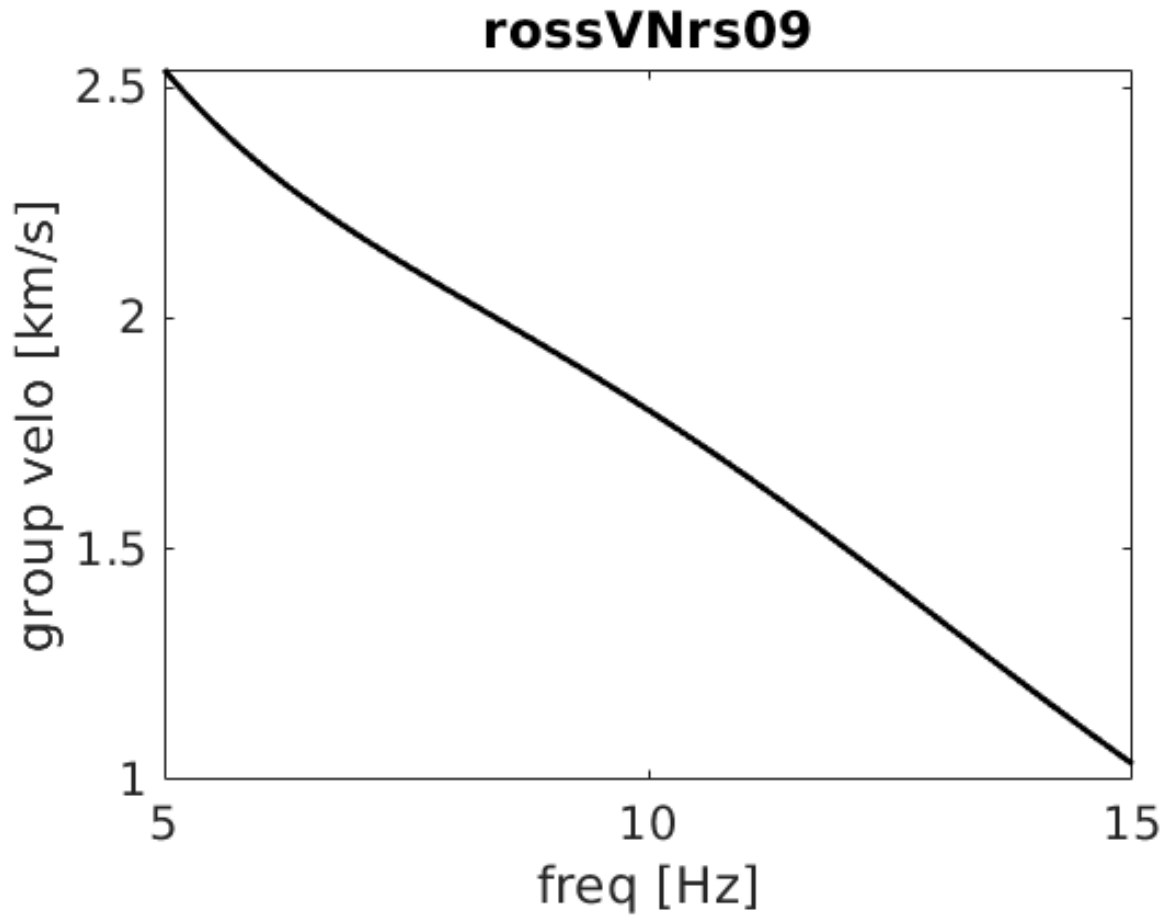


**Figure 2.10:** Group velocity as a function of frequency in Hz for the RS09 velocity model. The subtle departures from a linear trend propagate to more curvature changes with increasing distance.

delayed that its tail would fall outside the typical 10.0 seconds event window. This suite of time-frequency dispersion curves as a function of range are then used to estimate the source-receiver distance for an event by summing the pixels along each trace in an acceleration power spectrum spectrogram. Each curve is also allowed 0.2 seconds of pre-arrival and 0.7 seconds of post-arrival lag relative to the defined surface wave arrival to account for error in the automatic surface wave arrival time picks. The distance and lag combination with the largest sum is considered the best fit and the range is recorded for the event. This method is prone to errors but produces reasonable results in agreement with the arrival time difference method. Errors arise for a variety of reasons. The crude trace optimization that selects the best-fit curve is susceptible to poor fits from spectral noise and could be improved by selecting a most-likely fit instead. Overlapping icequakes or multiple distinct icequakes within the event observation window can also cause errors in this method. It is also highly dependent on a crude 1D firm velocity model derived from the RIS interior which likely is appreciably different from those near the grounded margins or even eastern RIS more broadly (Diez et al., 2016). This ranging method shows promise as a suitable single station location method but needs to be crafted into a more sophisticated inverse problem which falls outside the scope of this work but will be a priority for future research.

## **2.4 Icequake Swarm Classification**

Icequakes occurring in swarms broadly fall into four categories, referred to in this text only as type A, B, C, or D because their source mechanisms cannot be conclusively determined unless a more focused seismic deployment is conducted in concert with other geophysical surveys. However, given the information available, likely source mechanisms are interpreted and discussed. The icequake types are differentiated by their combination of frequency content, timing in the tidal cycle, and correlation to environmental conditions. Swarms are mostly comprised of one type of event, but swarms with several types of events or overlapping swarms exist in the data. It is important to note that these event types do not represent all seismicity that is recorded by stations near the grounding line. Non-repeating icequakes, and local or regional earthquakes are present in the

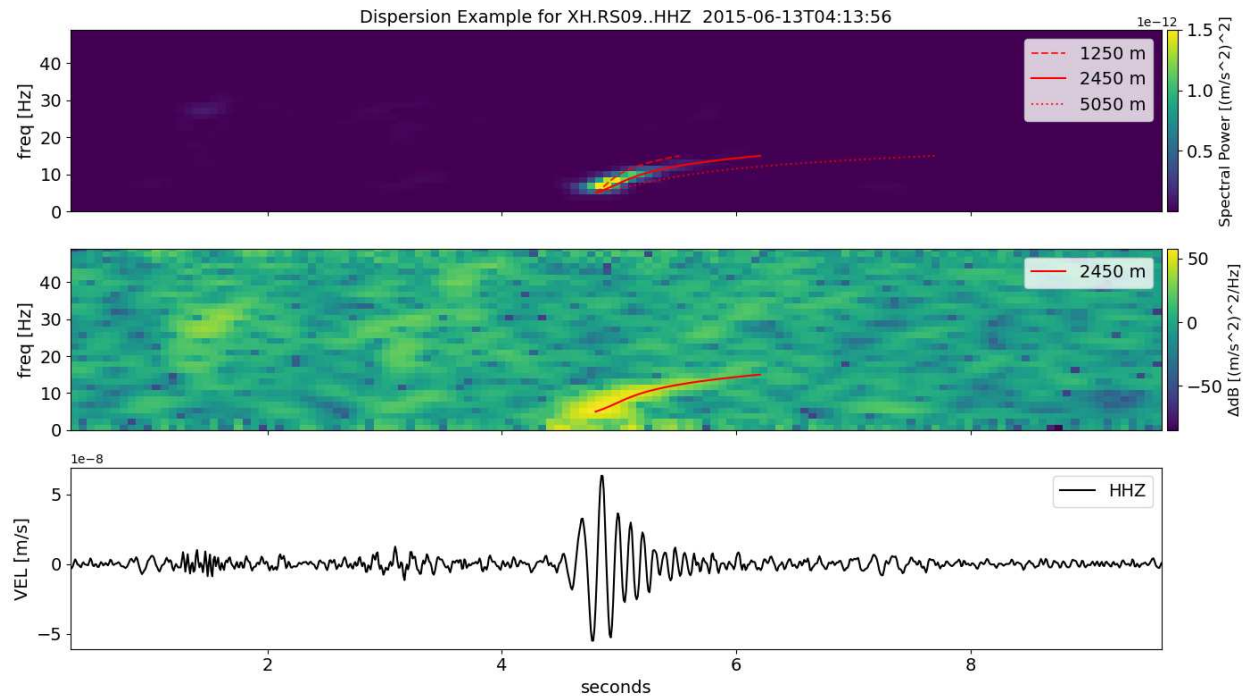


**Figure 2.11:** Example event showing the power spectrum spectrogram (top) with the best fit dispersion trace (solid red) along with two dispersion traces for other ranges (dashed and dotted red). The PSD spectrogram demeaned by frequency bin (center) shows more detail in the signal.

data but are not captured by the detection scheme because it uses cross-correlation detection and will only add repeating events to the catalog. However, because of the abundance of events in a swarm and the daily periodicity of swarms at the grounded margin, a majority of seismicity at the grounded margins will fall into one of these types.

Located events can be procedurally classified into the four types using simple machine learning tools. To test this, certain measurements from the event catalog were selected as input for a Gaussian Mixture Model which is a probabilistic unsupervised machine learning method similar to K-means clustering that allows for the identification of a number of sub populations within data. This is done by ellipsoidal clustering based on euclidean distance in multi-dimensional data sets. In this case useful metrics distinguishing event types that are tracked in the event catalog and selected for use in the Gaussian Mixture Model are the signal-to-noise ratio, phase arrival time difference, frequency index and its constituents, the dominant frequency, and back azimuth. Since this method is unsupervised, the only other input before training is the desired number of clusters

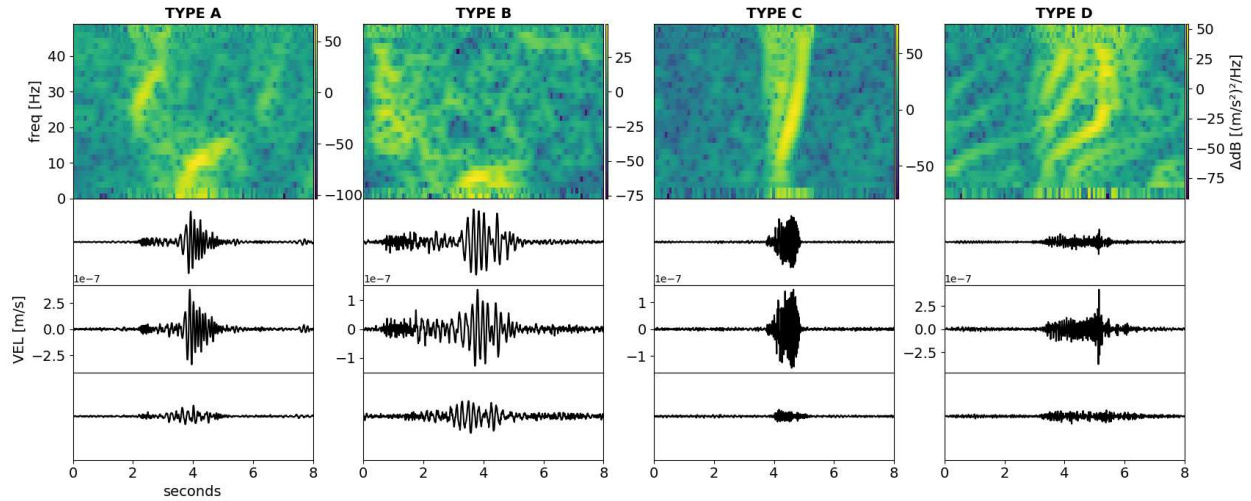


**Figure 2.12:** Examples of the four types of events from the located event catalog. Spectrograms are acceleration power spectral density plots demeaned at each frequency bin to improve clarity. Seismograms are rotated to ZRT domain, bandpass filtered 5-35 Hz, and scaled to have equal vertical limits for each channel.

(3 in the case of all stations of interest except RS17 which has 4). After training the model, it can be refit to the same or more data to assign labels to each event. The labels are meaningless until manual assignment of each of the 3 or 4 labels to an interpreted event type. This method is beneficial for classifying the icequake types because many of their measured properties overlap and there are far too many events to perform robust quality control on a business logic methodology, let alone attempt to manually classify events. Results from automatic classification could also be extended to apply additional signal processing techniques only to certain types of events. In this work it is useful for determining when types of events are happening and what the relative number of the various event types are.

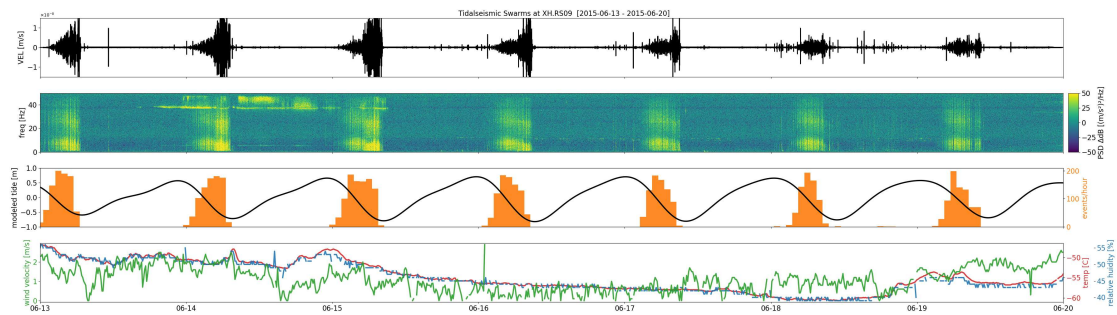
### 2.4.1 Type A: Falling Tide

By far the most common type of event recorded at stations near the grounding line are type A events. They are visually estimated to be more than 95% of detected events. These occur in swarms during falling tide at all times of year and are not significantly affected by weather conditions or seasonal changes. Their frequency content is bimodal with a strong peak centered  $\sim 8$  Hz and a subtle peak centered  $\sim 30$  Hz. These peaks migrate slightly during and between

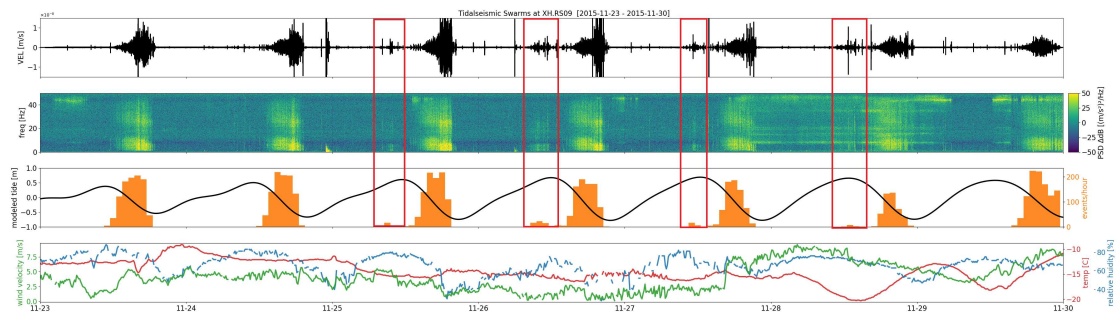
swarms. In timeseries, the subtle peak arrives up to several seconds before the strong peak, which are interpreted to be the body and surface (Rayleigh) wave arrivals respectively. The surface wave arrival is almost always visibly dispersed with higher frequencies arriving later. Some signals are clear enough to also show dispersion at lower frequencies ( $<2$  Hz) which is due to sensitivity to the water cavity beneath the ice shelf. Interpreting these icequakes to be sourced from mixed-mode, near-surface crevasses is consistent with observations here and in other similar work (Mikesell et al., 2012). The timing relative to the tidal cycle of type A swarms is favorable for near surface tension as ice near the grounded margin is flexed downward. The relative amplitudes of body and surface waves shows that signals are dominated by surface wave energy which is indicative of a near-surface source. However, if these events were a simple mode-I surface crevasse like might be expected in these flexural conditions, there might also be a noticeable correlation of seismicity with cooler air temperatures since the crevasse would be exposed to the atmosphere and the cold air would enhance brittle failure and thermal contraction. The lack of a noticeable correlation to absolute air temperatures or a seasonal dependence of this type of event could be because crevasses have a more shear sense of failure and are not open to the atmosphere, that thermal embrittlement is not important to their seismogenic behavior, or that they are sourced at sufficient depth not to be affected by seasonal-period ( $<1$  year) changes in air temperature.

#### **2.4.2 Type B: High Stand**

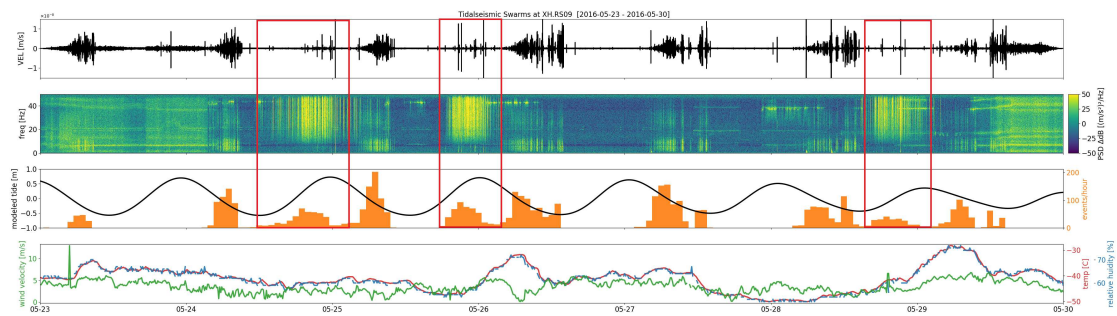
Type B events are broadly similar to type A in many respects. They also have bimodal frequency content, showing spectral peaks near  $\sim 8$  Hz and  $\sim 30$  Hz. These arise from a similar pattern of body wave arrivals in the higher frequency band followed by a surface wave arrival in the lower frequency band. The surface wave is dominated by Rayleigh wave particle motion similar to type A events. However, the relationship to tidal phase for these events is distinctive; they tend to occur during the exceptionally high tides of spring tide cycles, sometimes referred to as “king tides”. Also, the relative amplitudes of body to surface waves are nearly equal, where as type A events have much more surface wave energy relative to body wave energy. This is largely



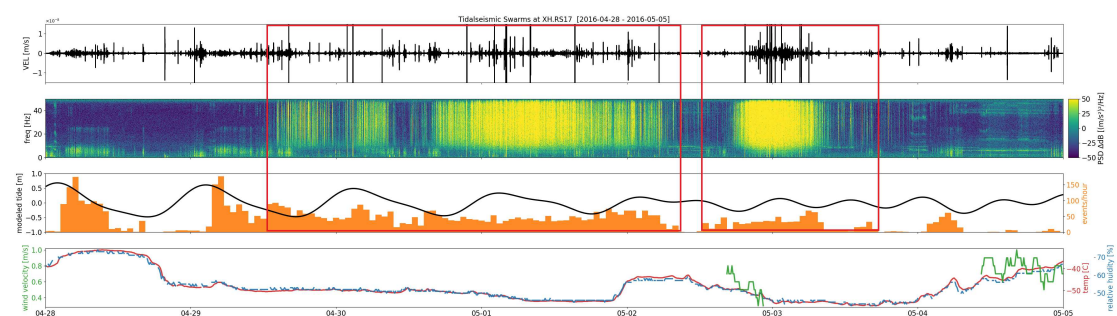
(a) Type A



(b) Type B



(c) Type C



(d) Type D

**Figure 2.13:** Plots of 7 days of seismicity to highlight the four types of events. The top plot is a vertical velocity seismogram bandpass filtered 3-35 Hz with all figures having equal scaling. The spectrogram is a PSD demeaned at each frequency bin. Cross-correlation picks are shown in 1 hour bins along with modeled tidal range. Red boxes highlight other swarm types apart from type A.

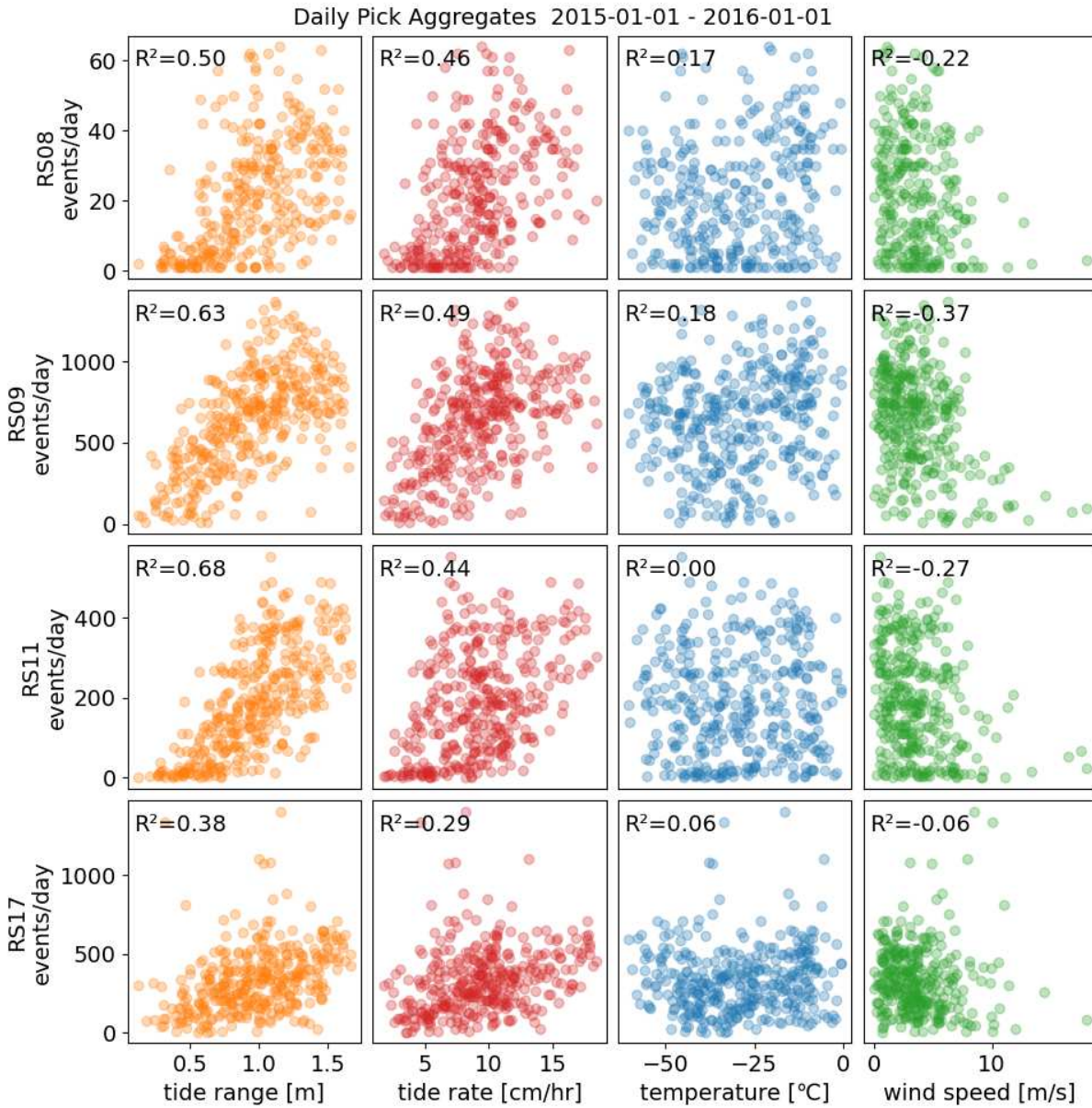


**Figure 2.14:** Scatter plots showing correlation of tidal range, tidal rate of change, air temperature, and wind speed at stations of interest. R-squared values for linear regressions of each plot are shown.

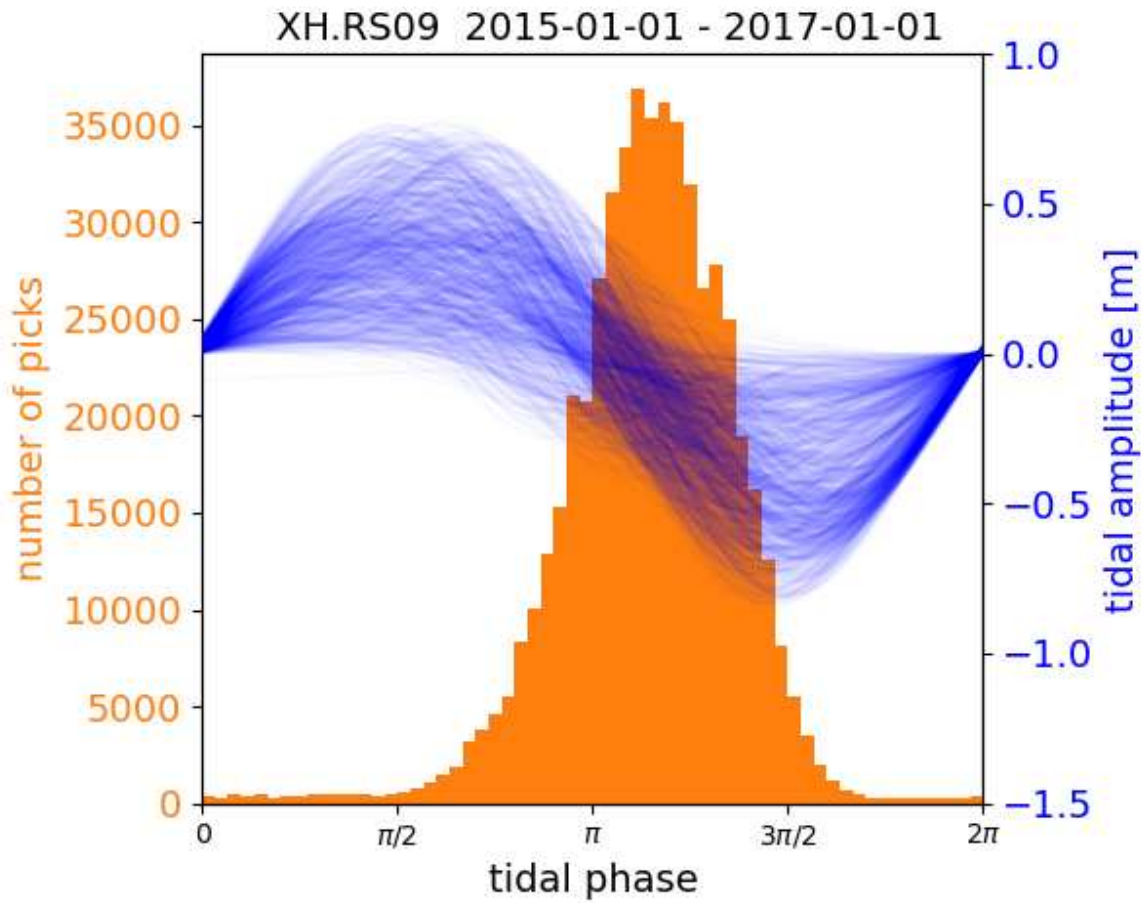


**Figure 2.15:** Histogram of cross-correlation pick counts binned by timing relative to tidal phase.

because type B events have low-amplitude surface wave energy compared to the others, but the high-frequency arrivals are particularly clear in many cases. This could indicate that these events are due to sources from deeper in the ice shelf that would preferentially excite body waves and have reduced excitation of surface waves. Possibilities include basal contact with a bedrock asperity, basal crevasse propagation, or ocean water infiltration along the basal surface. A mechanism cannot be conclusively determined with the observations in this work, but the basal crevasse propagation source is favored because of the similarity to type A events which are interpreted to be from surface crevasse propagation. This event type is less common in the located pick catalogs because the weak surface wave results in a low signal-to-noise ratio and therefore is often filtered out with the intent to limit the number of low-quality locations.

### **2.4.3 Type C: Cold Snap**

Type C events are distinct from the other event types in that their occurrence is correlated with colder temperatures and show at best only a weak association with tides. When the detection scheme is applied to stations that are far (more than 25 km) from the grounding line, they are dominant or only type of repeating seismicity that is detected. They have broadly distributed frequency content with a single peak near  $\sim 15$  Hz and no clear separation of the body and surface arrivals visible in spectrograms or seismograms. These signals are extremely polarized and have little to no transverse energy after seismogram rotation. Their character resembles that of a slightly dispersed impulse which indicates the wave train has not propagated through much material and therefore has a very near source. These events do not have a strong correlation to the tidal cycle, but do occur preferentially during rising tides. Their swarms can last multiple days with periodic increases in seismicity within swarms during rising tides. Unlike the other types of events, type C events have a strong environmental control (Figure 2.16), occurring only during the austral winter when conditions are cold ( $< 30^\circ$  C). They also tend to occur more often during periods of prolonged drop in temperature. For a so far unknown reason, these events occurred much more often during the second winter of the RIS/DRIS deployment (Figure 2.17). The correlation with

cold temperatures implies that these events are affected by atmospheric temperatures and are thus sourced in the very near-surface. Their minor correlation with rising tides indicates that the source mechanism also secondarily enhanced by tidal forcing. This fact, combined with their observation across all stations on the shelf, indicates this correlation is related to the shelf slope, rather than the tidal flexure that drives type A events or tidal heights that govern type B events. Their source mechanism is also likely related to processes in the firn because active brittle failure in blue ice is much less prevalent near mid-shelf stations where type C events are observed as supported by the much smaller repeating event counts at mid-shelf stations and the reduced dynamic forcing of the stress field compared to ice near the grounded margins.

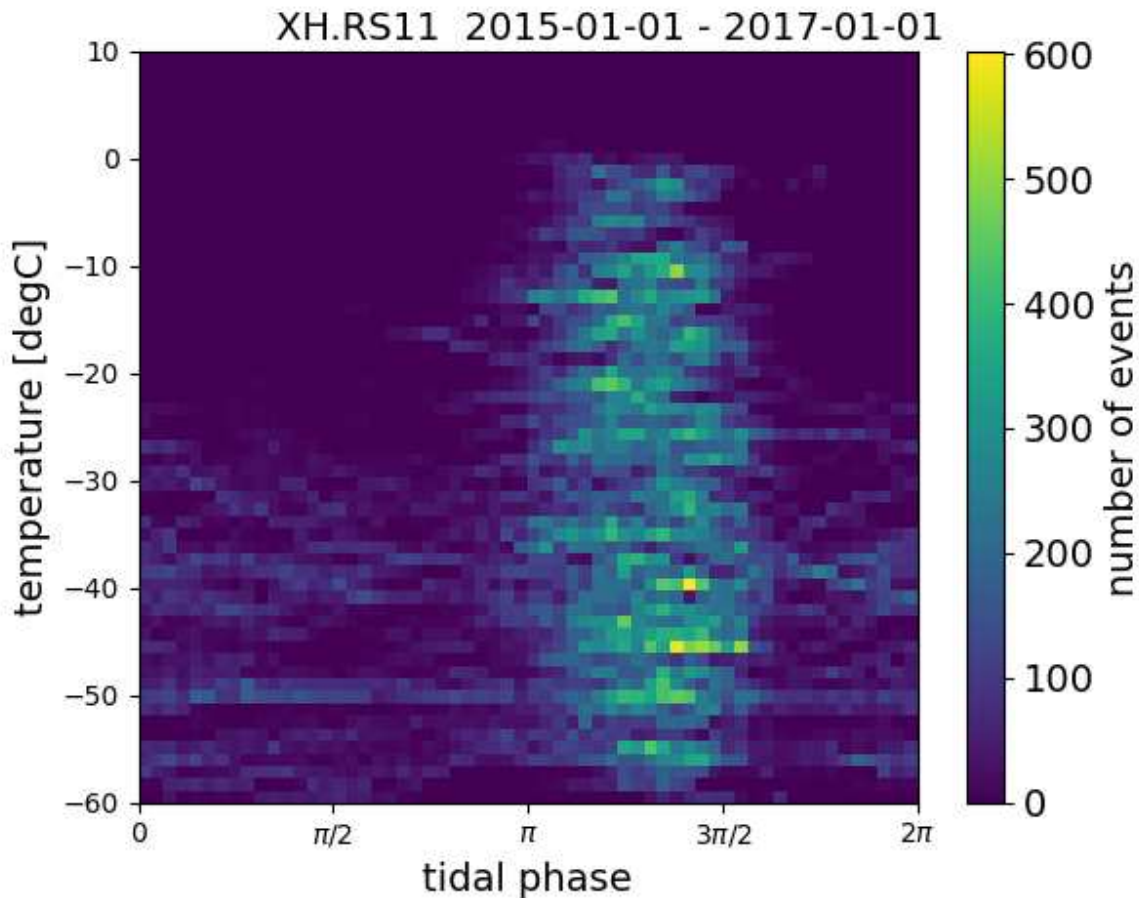


**Figure 2.16:** 2D histogram of cross-correlation picks at RS11 showing the type A events centered  $\sim 3\pi/2$  and the type C events dispersed when temperatures are below  $-30^\circ\text{C}$ . The slight preference for type C events can be seen near  $0$  and  $2\pi$ .

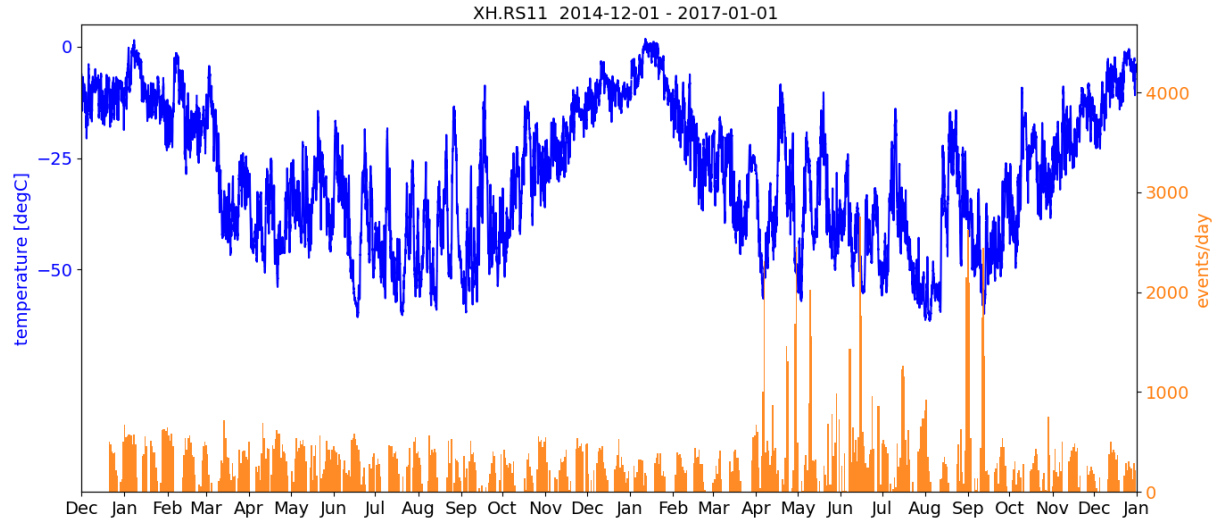


**Figure 2.17:** Plot air temperature and cross-correlation pick counts binned by day showing spikes in seismicity (mostly type C) during the second winter of the RIS/DRIS deployment.

#### 2.4.4 Type D: Tremor

Event type D are icequake tremors that are common at RS17, uncommonly observed at RS11, and rare elsewhere. They are easily identified by a long sweep in seismicity with slowly increasing frequency, lasting several seconds that often ends with a high-amplitude impulse ranging the rest of the higher frequencies. These will often exhibit harmonic spectral signatures making their frequency character the most unique of the four event types. These are most difficult to interpret because they do not exhibit clear phase arrivals or predictable dispersion characteristics. The problem is further complicated as RS17 is located on an ice rise where compressive, shear, and tensile failure are occurring locally as ice flows around the pinning point. One possible mechanism is hydraulic fracturing at the basal surface, which is consistent with the broad frequency distribution, lack of clear surface wave phases, and harmonic character which is similar to that observed in other glacial settings (Helmstetter et al., 2015). Another possible mechanism is compressive failure where the harmonic character results as ice briefly slides at an angle to accommodate shortening.

# Chapter 3

## Tidally Induced Icequake Swarms

This chapter serves as a self-contained scientific publication aimed at an audience already familiar with most material presented in the background chapter.

### 3.1 Abstract

Repeating swarms of tidally induced local cryoseismic events were recorded by broadband seismographs deployed on the Ross Ice Shelf, Antarctica from late 2014 to early 2017. The swarms are observed exclusively at stations near the grounding line or at mid-shelf pinning points. They occur in phase with modeled tidal cycles and produce peak seismicity at  $90^\circ$  phase lag following high tide. Swarms commonly last over six hours, typically exhibiting a gradual increase in event intensity and rate of occurrence before ending abruptly. Swarm intensity is well correlated with the modeled tide range but typically not sensitive to seasonal or environmental conditions. Event waveforms show repeating families of similar events originating from distinct source regions, likely crevasse fields resulting from tidal flexure. Our work constrains source regions and describes possible seismogenic processes. The primary types of events are dominated by Rayleigh waves, so we use surface wave analysis to constrain their location using a single station. Preliminary results suggest a shallow source for most seismicity, but other types of swarms are present which may have an englacial or basal source. We hypothesize that the main type of swarms arise from increased tensile stress at the surface of the RIS during falling tide as bending occurs near the grounded margins. This is not an original observation, but is the first time these events have been identified in new data from the Ross Ice Shelf. We anticipate that these observations will provide further insight into the dynamics and brittle properties of the ice shelf and serve as a useful comparison for similar activity in other glacial environments. This should also guide efforts to observe and utilize this phenomenon to improve understanding of other tidally stressed glacial masses.

## 3.2 Introduction

Ice shelves are mature glacial masses that form when grounded ice flows into the ocean and persists over many years. Their presence results in a so called buttressing effect which is a crucial component affecting ice shelf mass balance, stability of entire glacial networks, and global mean sea-level rise (Paolo et al., 2015; Furst et al., 2016; Robel et al., 2017). The buttressing effect slows the flux of glacial material across the grounded margins where ice shelves are pinned to continental glaciers. These marginal zones can account for much of the circumference of an ice shelf and are host to dynamic activity associated with the advance of land ice into the ocean. Glacial ice can be deformed or otherwise modified as it crosses the grounded margin and imprinted with fractures that seed the geometry of iceberg calving and ultimately ice shelf collapse. The diverse processes in play at these margins can result in seismicity when mass movement, deformation, hydraulic activity, or brittle failure are occurring and the physical properties of the ice are favorable for seismic propagation (Aster and Winberry, 2017). Often glacial seismicity is modulated by ocean tides, as noted by seismograph deployments on other ice shelves and in the ice stream regions of West Antarctica (Osten-Woldenburg, 1990; Anandakrishnan and Alley, 1997; Hulbe et al., 2016; Hammer et al., 2015; Lombardi et al., 2016; Barruol et al., 2013). This is a commonly observed effect of the persistent periodic forcing from ocean tides that acts on all marine terminating glacial systems (Padman et al., 2018). However, constraining external forcing and source mechanisms remains an area of active research.

Here we report observations of tidally forced icequake swarms occurring at the grounded margins of the Ross Ice Shelf (RIS), Antarctica. Our findings show distinct populations of swarms differentiated by their frequency content and timing relative to the tidal cycle. Some populations only occur during certain times of year or during periods of certain environmental conditions. We see that most seismicity is primarily governed by tidal forcing with no clear association to environmental factors. However, smaller populations of seismicity are present that are primarily forced by cold temperatures and are only enhanced by tidal controls. These swarms occur daily through-

out the entire record of seismic data show that this phenomenon can provide a reliable pulse for monitoring activity at the grounded margin as it evolves over time.

## **3.3 Data**

### **3.3.1 Seismic Data**

We use seismic data collected by the RIS (Mantle Structure and Dynamics of the Ross Sea from a Passive Seismic Deployment on the Ross Ice Shelf) and DRIS (Dynamic Response of the Ross Ice Shelf to Wave-Induced Vibrations) experiments which operated concurrently from installation in late 2014 to retrieval in early 2017 (doi:10.7914/SN/XH\_2014). We use only select stations from the RS array, which consists of 18 stations spanning the width of the shelf with average station spacing 100 km. The coincident DR array was not used because all of its stations are located in the interior of the floating shelf and are too distant from marginal seismic zones. While we examined data from other RS stations our discussion focuses on the stations RS08, RS09, RS11, and RS17 which were all deployed on or near grounded locations. The seismic RIS network will be referred to as RS to prevent confusion with acronym RIS for the Ross Ice Shelf.

The stations of interest focused on in this study (RS08, RS09, RS11, and RS17) were equipped with a Trillium 120PA broadband seismometer installed in a shallow vault, with the exception of RS08 which used a Trillium 120 PH sensor and was buried at 2-3 m depth in the firn (and further buried by accumulation during deployment). Both station setups sampled at 100 Hz. Data was accessed via the Incorporated Research Institutions for Seismology (IRIS) Data Management Center (DMC) web services and downloaded as day-long SAC files after server-side instrument response correction to velocity units and demeaning. Processing of seismic data was done with custom software written in the Python programming language aided by the open-source ObyPy and REDPy packages (Krischer et al., 2015; Hotovec-Ellis and Jeffries, 2016).

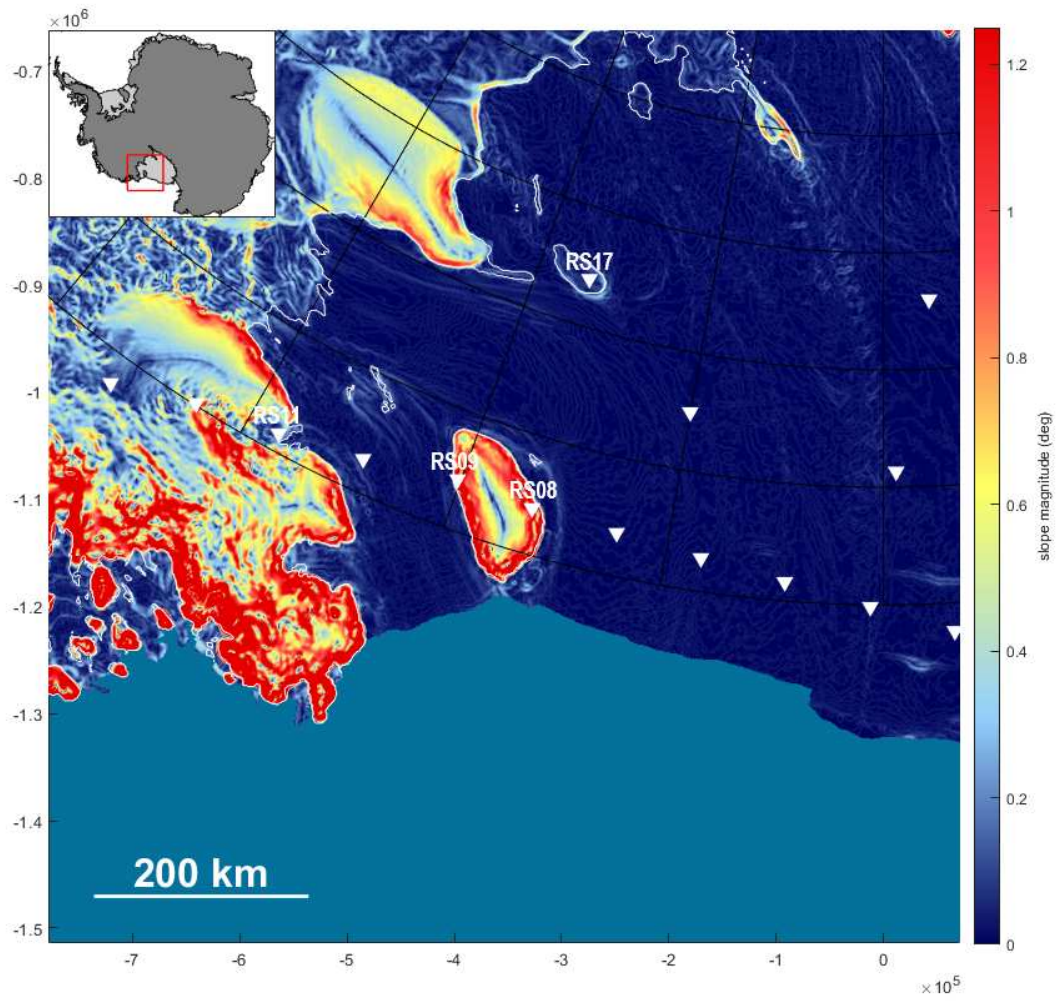


**Figure 3.1:** Map of ice surface slope derived from Bedmap2 and XH network stations. Seismic stations are shown as white triangles. Stations of interest for this study are labeled. The mapped grounding line is shown in white.

### **3.3.2 Tidal Data**

Synthetic tidal time series containing all tidal constituents resolved at 10 minute intervals were generated for each station using the Tide Model Driver MATLAB package and an input model (CATS2008) specifically made for tides in the Ross Sea (Padman and Erofeeva, 2005; Padman et al., 2002). Since all stations of interest are technically grounded, we run the model for the nearest valid point toward the ocean. Importantly this model assumes a hydrostatic surface up to the grounding line and does not consider the presence of ice (Padman et al., 2003; Rignot et al., 2000). Therefore it does not account for flexure of the ice shelf that is certainly present at the points used. So the tide heights we report overestimate the true value but are still useful to show tidal phases and relative changes accurately. The Ross Sea has a large tidal form factor, meaning the diurnal component of tides dominates and produced a single high and low tide each day, unlike most other places on Earth where semidirunal component dominates and produces two high and low tides each day (Padman et al., 2018). In the Ross Sea Embayment, typical spring tide diurnal cycles are over 1 meter, while during some neap tides the range can be negligible for several days. As the various tidal phases migrate and stack, the length of each cycle expands and contracts so at times we consider tidal phase which is extracted from the time series by finding successive positive zero-crossings and assigning phase values for each point between.

### **3.3.3 Environmental Data**

Records from the Antarctic Automatic Weather Station (AWS) project provide the atmospheric measurements used in this work (Lazzara et al., 2012). We use quality controlled 10 minute time series of air temperature, pressure, wind speed, wind direction, and relative humidity from the AWS stations named Margaret and Gill which are both located on the shelf interior. Margaret is the primary AWS station we use because of its closer proximity to seismic stations of interest near the grounded margins. During processing the placeholder flags for missing values and rare erroneous data are removed. Weather data is used to determine if types of seismic events have correlation to wind or temperature which indicates whether they are sourced at or very near the

surface. Wind measurements also prove useful in assessing whether periods of high wind explain noisy trends in seismic data processing.

## **3.4 Methods**

### **3.4.1 Signal Analysis and Event Detection**

Icequake swarms were first observed in the seismic data from month-long spectrograms by (Chaput et al., 2018) that showed regularly repeating multi-hour windows of high frequency energy ( $>1$  Hz). Swarms with abundant distinct icequakes are observed at the three stations of interest (RS09, RS11, RS17) and to a lesser degree at RS08. Examining individual events in swarms we see four basic types of events, referred to in this work as type A, B, C, and D. Type A is by far the most abundant type of icequake (visually estimated to be more than 95% of the catalog). It has bimodal frequency content consisting of a weak body wave arrival in the 25-35 Hz band followed several seconds later by a surface wave arrival in the 5-15 Hz band. Surface waves are dominated by Rayleigh wave particle motion, but some larger signals also show a preceding Love wave arrival after synthetic rotation of the seismograms. This is demonstrated by computing particle motion linearity, circularity, and sphericity measurements for event particle motions and observing a transition from linearity to circularity as the Love then Rayleigh phases pass the receiver (Aster et al., 1990). Type A events display dispersed surface waves showing delayed arrivals for higher frequencies resulting from normal Rayleigh dispersion arising from the steep velocity gradient present in the firn. Curiously, the body waves also show dispersion at higher frequencies. Clean signals sometimes also show delayed arrivals for lower frequencies ( $<2-3$  Hz) due to sensitivity to the water cavity beneath the ice shelf along the propagation path. Type B events are similar but have slightly lower frequency content, a higher ratio of body to surface wave energy, and no body wave dispersion. Type C events have broadly distributed frequency content with a single peak near  $\sim 15-20$  Hz and no clear separation of body and surface wave phases. Type D events are observed primarily at RS17 and are unique by expressing gliding harmonic frequency content until an impulse-like end of the event.

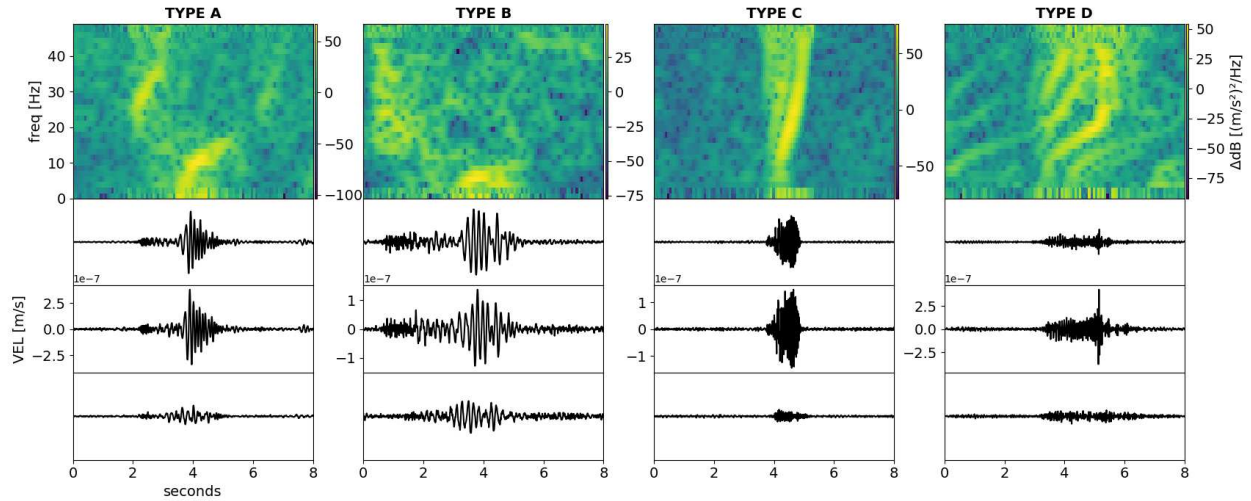


**Figure 3.2:** Examples of the four types of events from the located event catalog. Spectrograms are acceleration power spectral density plots demeaned at each frequency bin to improve clarity. Seismograms are rotated to ZRT domain, bandpass filtered 5-35 Hz, and scaled to have equal vertical limits for each channel.

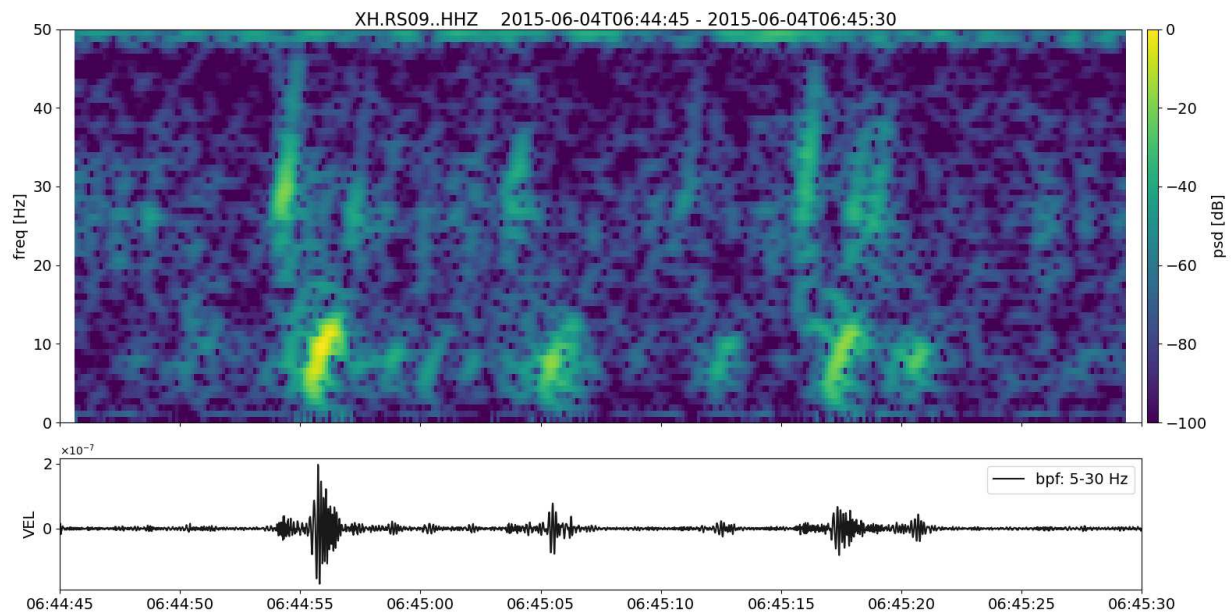


**Figure 3.3:** Example events from station RS09. The power spectral density plot (top) shows the signatures of the body waves (25-35 Hz) and surface waves (5-15 Hz) present in the seismogram (bottom). Surface wave dispersion from Rayleigh and water cavity effects are clearly visible. This plot shows average event density during a falling tide swarm with  $\sim 10$  events happening every minute.

A catalog of events is created to analyze swarm seismicity. Processing is done per station as the events of interest are highly local and thus not detectable by multiple stations. We use the python package REDPy (Hotovec-Ellis and Jeffries, 2016) to build an initial catalog to create event templates, then refine our detection with a second pass using a cross-correlation detector. Icequakes are initially detected in REDPy using a short-term average/long-term average (STA/LTA) trigger on vertical seismic traces bandpass filtered 5-35 Hz. The short term window is defined as 1.0 seconds and the long term window is defined as 8.0 seconds. The trigger is activated when the ratio rises above 6.0 and deactivated when it falls below 5.0. As events are detected they are clustered into families with a similarity threshold of 0.9. From the REDPy output 10.0 second templates are generated for each cluster by taking the mean of the lag-adjusted seismograms of up to 300 cluster members. The library of templates is then filtered to remove clusters with less than 15 members. These templates are used as input for the Obspy correlation detection function which associates events to the most similar template with a minimum similarity of 0.7. Although events can occur so frequently that they often overlap, we limit correlation detections to one event every 5.0 seconds. These correlation detections are used to determine the relationships to tidal and environmental forcing. The STA/LTA trigger catalog and the cross-correlation pick catalog are both processed to extract swarm information by defining a swarm as a group of at least 15 triggers/picks without 20 minutes passing between any of them.

### **3.4.2 Estimating Event Locations**

While single station event location with broadband sensors is often inaccurate, the large quantity of correlation detections allows us to constrain the location of events which aides in interpreting source mechanisms. Event epicenters and local magnitude are estimated for each correlation detection with cross-correlation similarity of at least 0.8. Source locations are determined with polarization analysis to determine back azimuth (Vidale, 1986; Aster et al., 1990) and two methods of estimating source-receiver distance. The first ranging method is a simple arrival time difference using automatically picked time for the body and Rayleigh phase arrivals based on signal-to-noise

thresholds and assumed velocities of  $V_p=3870$  m/s (Walter et al., 2015b) and  $V_{\text{rayleigh}}=1550$  m/s (Olinger et al., 2019). The second ranging method finds a best-match among forward modeled dispersion curves for various distances to the observed dispersion of Rayleigh waves. The modeled dispersion curves are generated using the OASES software package with a velocity model including the firn model of (Diez et al., 2016) on top of ice thickness, cavity, and bedrock depth values derived from Bedmap2 (Fretwell et al., 2013) while assuming a seismic source at 20 meters depth. The dispersion ranging method is under-determined because it depends on a velocity model, source depth, and distance to event which are all unknowns. The results from this method are further complicated by the presence of cluster and azimuthal-dependent disagreement between the two estimates of distance, likely due to effects from crevasse-induced anisotropy and spatial variation of the true seismic velocities. Dispersion ranging results are used as an indicator of the relative source-receiver distances but we recognize its limitations in producing accurate locations. A more advanced Monte-Carlo method could be applied to better constrain input parameters and improve accuracy. For each event with a location estimate, the local magnitude and moment magnitude are computed (Stein and Wysession, 2009; Hanks and Kanamori, 1979). Estimated event local magnitudes for type A events range from -4 to -2. It remains unknown what role anisotropy plays in the propagation of these signals. We should expect that all grounded margins are coincident with glacial fabrics capable of producing anisotropy, but icequake events may be weak or near enough that their energy does not pass through enough material to become significantly affected before attenuating completely. This further complicates assessing the accuracy of any single station location method that relies heavily on a velocity model or forward modeled wave propagation.

## **3.5 Results and Discussion**

### **3.5.1 Repeating Icequake Events**

Highly similar seismograms are observed within and between swarms indicating that individual or closely associated sources are triggering repeatedly, often for extended periods of time. The lifespan of event clusters varies, with some lasting the entire deployment while others will only be

observed during a single swarm or during a single tide cycle. Since we are able to stack repeating events to create templates and implement a correlation detector, we are able to gather a more accurate event count than would be possible with an STA/LTA method alone. However, the number of events recorded by the station is still under-counted because they are so frequent during some swarms that two or three events may overlap and hinder our detections. Either way, counting events provides limited insight because this seismicity is a spatially distributed phenomenon observed at a single station, often with poor location and size constraints. The fact that we observe many clusters with many members supports the interpretation that most clusters are sourced from crevasse or other repeating fractures where the event epicenter and propagation path do not change appreciably between events. For events (type B) that are possibly sourced at the basal surface, repeating events support an interpretation of basal crevasse sources or sticky pinning points.

### **3.5.2 Tidal Forcing of Icequakes**

As noted previously, type A events represent the vast majority of seismicity detected at the grounded margins (estimated at >95%). This type of seismicity only occurs during periods of falling tide (Figure 3.4) and has no apparent correlation with air temperature. Falling tides are not accompanied by these swarms only when tidal range is small (<0.2 m). It also occurs exclusively at stations near the grounded margins. Therefore, type A seismicity is clearly driven by tidal forces, likely by increased tensile stress due to flexure of the ice shelf given its timing in the tidal cycle when the tides are lower than equilibrium and floating ice is depressed relative to grounded ice. Type B seismicity occurs at the crest of high tides during spring tide cycles and is also exclusive to stations near the grounded margins. While this type of seismicity is clearly thresholded by the tidal cycle, it may actually be forced by gravitational stresses advancing glacial ice over the grounding line, with high stand tides reducing normal stresses at or near the ice shelf base. In this case ocean tides may govern type B seismicity by reducing basal drag to the point where it can slide. Type C events are mainly correlated with cold (winter) temperatures and show enhanced activity during rising tides at stations near the grounding line but not at stations in the shelf interior. Again this

type of event is not strongly affected by tides but rising tides seem to create a favorable stress state for them, either from compression of the near-surface or tension near the basal surface.

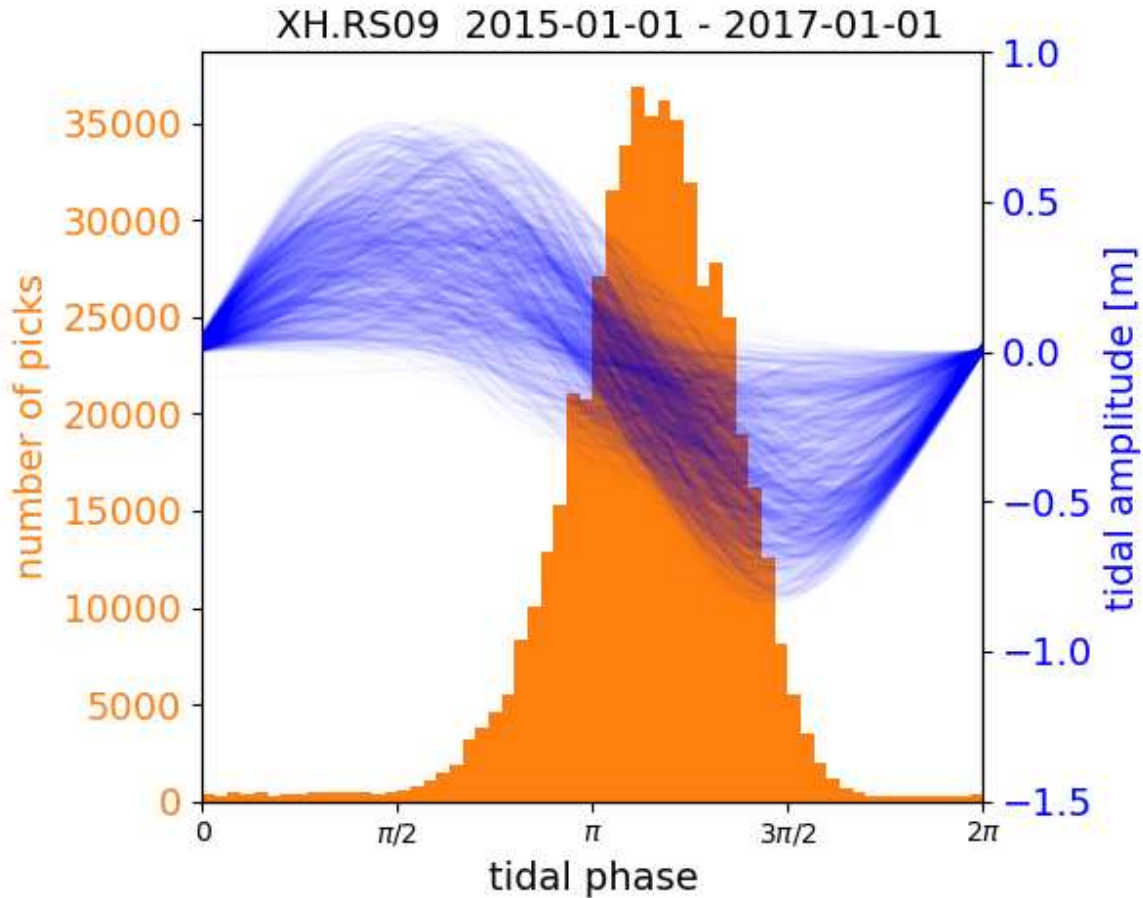


**Figure 3.4:** All tidal cycles and event counts relative to tidal phase at RS09 from 2015-2017.

### 3.5.3 Interpreting Icequake Types

I hypothesize that type A events are sourced from near-surface crevasses or fractures. This interpretation is supported by the high surface wave to body wave energy ratio, the timing in the tidal cycle when the near-surface experiences large tensile strain rates, and observed presence of surface features near stations where type A events are recorded (similar to (Barruol et al., 2013)). These events must be sourced from a depth of at least several meters because there is no apparent correlation with air temperature. Type B events are likely sourced from deep englacial fractures

or basal crevasses (similar to high frequency events in (Lombardi et al., 2016)). Their lower ratio of surface to body wave energy implies they at least have a deeper source compared to type A events. Their timing at the crest of large high tides is also consistent with a source in the lower half of the ice shelf thickness since this is under maximum tensile stress at that time. The similarity in frequency content and phase separation of type A and B supports that both are mostly mode-I (extension) crevasse source, whereas basal stick-slip or inland surges of ocean water would more emergent and low frequency compared to the type A events. Type C events are likely sourced in the very near-surface firn. They are only detected in the austral winter and only in large numbers during particularly cold periods, which implies a very near surface source (similar to (MacAyeal et al., 2019)). This interpretation is also supported by observing them at mid-shelf stations in addition to those near the grounding line meaning their source cannot be exclusive to the grounded margins. A likely source mechanism for these events is settling or compaction of the firn. Curiously for an unknown reason type C events are much more common during the second winter of the seismic deployment. This could be due to periods of snow accumulation which would drive firn compaction, but precipitation is not tracked in the weather data considered in this work. Type D events are gliding harmonic tremors commonly recorded at RS17 and rare at the other grounded stations (similar to ()). They are also forced by increased tensile stress during falling tides like type A, but must have a different source mechanism. It is possible that these events occur from a more shear sense of brittle failure than type A does, which could cause them to creep before triggering the main impulse, explaining their harmonic frequency content (similar to a short-lived version of events in (Martin et al., 2010; Lombardi et al., 2016)).

### **3.6 Summary**

As ocean tides exert flexural forces on grounded margins the Ross Ice Shelf it alternates between tensile and compressive stress regimes at its surface and base. At the same time ocean tides can temporarily reduce the basal friction and allow the bulk mass to advance. This results in several types of seismicity linked to tidal phasing. By far the most common, designated type A are falling

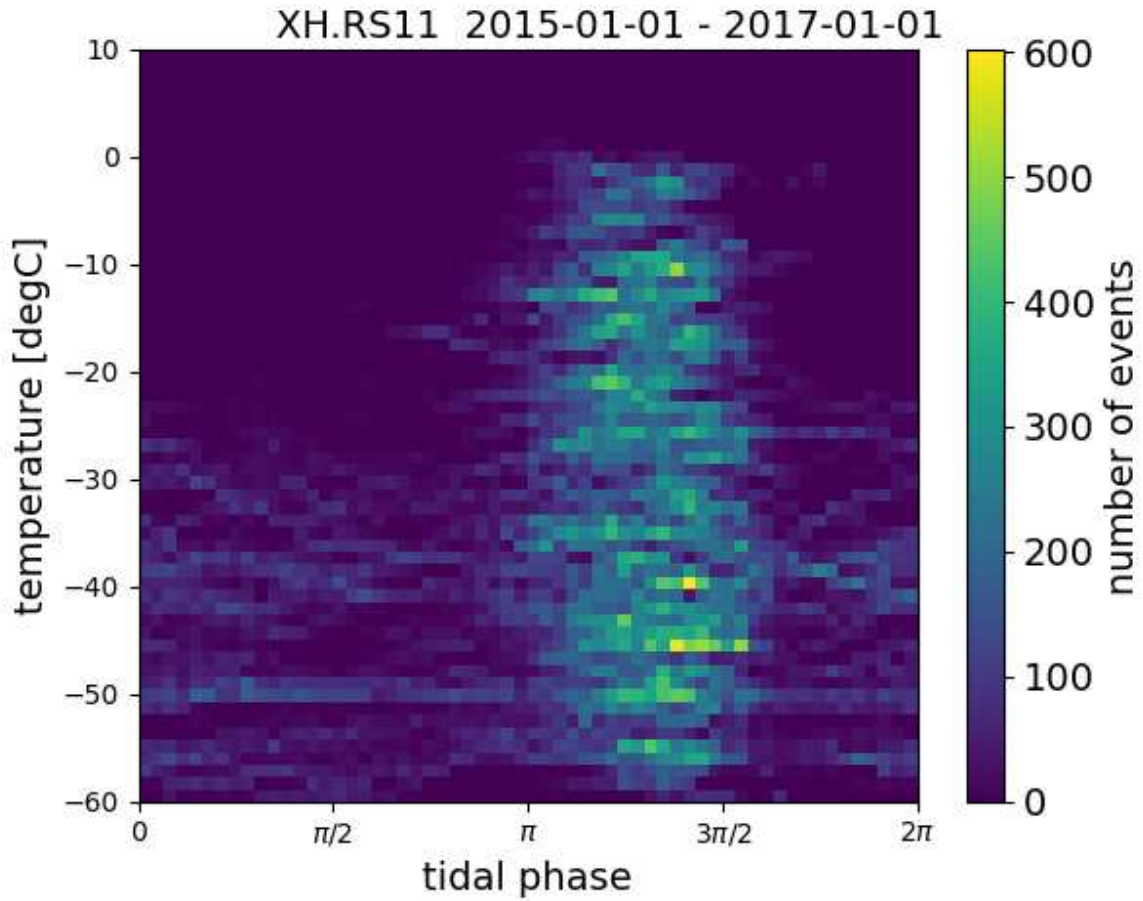


**Figure 3.5:** Density plot showing that separate populations of seismicity at RS11 depend on temperature thresholds and tidal forcing.

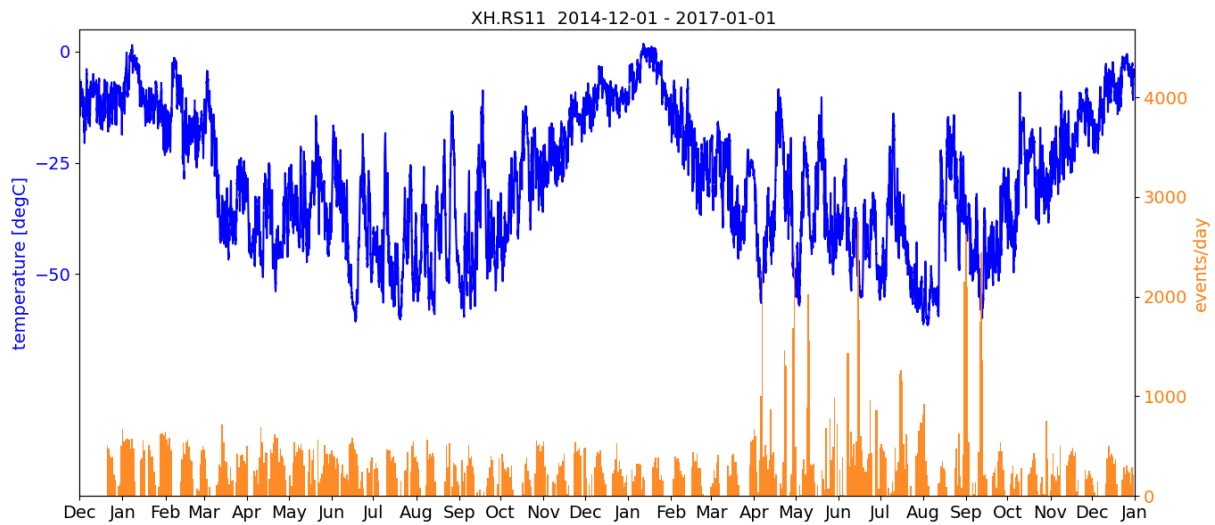


**Figure 3.6:** Timeseries of air temperature measured at AWS station Margaret and daily counts of correlation picks.

tide swarms that likely occur because increased tensile stress at the surface causes the propagation of crevasses near-surface crevasses or fractures. A lack of strong correlation with air temperature or seasonality suggests that type A icequakes have a source mechanism that occurs at sufficient depth to be decoupled from atmospheric influence. Type B events occur in swarms centered at the crest of high tides when tidal amplitude is sufficiently large. These events are similar in most respects to Type A events, but have frequency content that is shifted slightly lower and have larger ratios of body to surface wave energy, which suggests they are sourced from greater depth than type A events. We interpret these events to be sourced from activity near the basal surface, possibly fracture related to stick-slip advance of the ice shelf or propagation of basal crevasses. Type C events only occur in the austral winter during periods where air temperatures drop steadily and remain low for several days. These events have the larger seismogram amplitudes than other types and express impulse-like frequency content with little to no dispersion of the signal. Unlike other types of events described in this work they are observed at mid-shelf stations far from the grounding line. Since they are observed at all stations and appear to be sourced from very-near the seismic stations, we interpret these events to be related to activity in the firn triggered by cold snaps, either brittle failure of the firn from thermal contraction or firn compaction. Type D events are tremor-like signals observed primarily at RS17, located near the Steershead Crevasses where a (grounded) ice rise results in diverse surface crevasse structures and basal forcing. These events also tend to occur during falling tides like type A, but are distinguished by a sweeping harmonic signal that often ends with a pulse of energy in the higher frequencies. This type of event is more difficult to interpret because there are a number of phenomena that could cause it. Possibilities include creeping repetitive stick-slip advance of the basal surface or propagation of fluid filled crevasse. Since event types A, B, and D are strongly correlated with the tidal cycle and not observed in significant numbers at mid-shelf stations we can further support that flexure of the ice shelf at its grounded margins is major driver of seismicity and therefore brittle fracture and weakening of the ice shelf. This does not need to occur at a traditional grounding line where ice is advancing into the ocean, but can also occur at ice rises like near RS17 or in shear zones like near RS09. The catalog of

events produced in our analysis is not comprehensive because of mismatch between network coverage and the spatial extent of marginal seismicity which is likely a common phenomenon so we cannot conclusively determine the relative abundance of the different types of events. We should expect that tides induce brittle fracture at all grounded margins of the Ross Ice Shelf and most other ice shelves. This is important because the fracture patterns imprinted on glacial fabrics as they advance over the grounded margin will remain as the ice moves closer to the calving front and eventually detaches from the glacial mass. Monitoring seismicity at the grounded margins of vulnerable ice shelves should be an objective for their studies moving forward. Heightened seismicity in these areas can indicate degrading integrity of an ice shelf before larger scale features are observable with imagery or radar observations. Additionally, improved understanding of the environmental conditions and perturbations that result in increased seismicity ice shelves will help forecast their response to modeled climate change scenarios.

# Chapter 4

## Discussion, Conclusions, and Future Work

### 4.1 Event Detection Performance

The seismic data processing scheme to extract repeating events was applied to 11 stations. Stations RS09, RS11, and RS17 show larger amounts of repeating local events compared to the rest of the array by one or two orders of magnitude (Table 4.1). Data from mid-shelf stations RS01, RS03, and RS18 at the boundaries of the network produced no valid templates, thus no correlation picks or located events. More icequakes were triggered by STA/LTA, caught by cross-correlation, and eventually located at RS09 than any other station by more than a factor of two. This is partially because this station truly records more swarm seismicity, but also because many parameters like those used in STA/LTA and cross-correlation threshold were tailored for RS09 then validated at other stations. These subjective parameters could have been determined on a per-station basis, but this would have introduced varying levels of bias, so the same set of parameters was applied to all stations. Two interesting fringe cases are RS08 and RS10. RS08 was identified as a station of interest because it is technically grounded and we should expect to detect similar swarm seismicity there as other stations near the grounded margin. Similarly, RS10 was near the grounded margin, but on floating ice. One possible explanation for reduced levels of recorded swarm seismicity at these two stations is that they were configured with the posthole sensor and buried at greater depth than the grounded stations at RS09, RS11, and RS17. Since the most common signal in the data is type A, which is dominated by Rayleigh waves, stations buried at greater depth will have a dampened sensitivity to these kind of events. This is because the Rayleigh wave energy is concentrated at the surface and decays rapidly with depth (Stein and Wysession, 2009). Another interesting observation is that station RS17 produces roughly twice as many clusters and templates than other stations. This is interpreted to be due to signals arriving

station	STA/LTA Triggers	Clusters	Valid Templates	Correlation Picks	Located Events
RS01	1,121	25	0	0	0
RS03	281	1	0	0	0
RS05	4,576	24	7	1,183	41
RS07	11,583	50	15	7,464	850
RS08	22,960	52	13	17,192	5,110
RS09	270,759	156	32	462,604	205,039
RS10	37,157	136	31	23,289	8,533
RS11	167,491	107	25	134,661	43,568
RS15	37,951	110	38	18,116	1,675
RS17	100,756	259	62	276,626	77,282
RS18	258	2	0	0	0
Total	654,893	922	223	941,135	342,098

**Table 4.1:** Result counts from the different stages in the processing scheme.

from a broad distribution of back azimuths. This makes geological sense considering its location on the Steershead Ice Rise where cryoseismic activity would be potentially happening on all flanks.

## 4.2 Tidally Induced Seismicity

Since icequakes occur when the ice shelf reaches a favorable stress state and ocean tides are a first-order control on the stress state of an ice shelf, most seismicity occurs with a preference to particular tidal phase, the timing relative to the tidal cycle (Figure 4.1. For mid-shelf stations near a rift, like RS05, seismicity occurs during falling tide when the shelf is in maximum slope and gravitational tension activates brittle failure within the rift or the melange filling it (Olinger et al., 2019). For other mid-shelf stations with no significant nearby cyrotectonic features, tidal correlation is either slight or non-existent. For stations near the grounding line, type A seismicity occurs during falling tide, after the tide has passed its equilibrium point. This supports the interpretation of flexural driven seismicity over gravity driven because seismicity is not occurring until the ice has passed its equilibrium point. Note that for these stations, the modeled tides are less accurate than for mid-shelf stations because of the assumption of a hydrostatic surface up to the grounding line. So this offset from the expected timing of peak seismicity could be due to the limitations of the tide model. A similar peak can be seen at RS07 which is  $\sim 70$  km from the grounding line and

~90 km from the ice front. It is not clear if this is due to local seismicity or particularly energetic events sourced near the grounding line, but the peak is small relative to non-tidally dependent seismicity so the phenomenon is rare either way. Peak seismicity at RS10 occurs preferentially during rising and high tides, but not during falling tides. This is curious given its proximity (~25 km) to the grounding line. However, many streaklines and mapped shear crevasses are between the station and the grounding line, making them much more likely to be the source. Also, the peaks at this station are also barely above the background seismicity make the effect of secondary concern. RS15 has a large number of events compared to mid-shelf stations, but no apparent tidal influence. This is likely because only type C events are observed at RS15 and with no effect from flexure, a tidal correlation is not observed. Most seismicity on the ice shelf seems to be driven by tidal forces as there are much greater correlations of tidal range and tidal slope (rate of tide drop) than there are with air temperature or wind velocity (Figure 4.2).

### 4.3 Event Locations

Epicenter locations were estimated for 342,098 cross-correlation picks. When mapped, picks are dispersed in clouds that indicate areas of increased seismicity, but do not reveal significant structure. This is because there is significant uncertainty in the methods of location estimates, making the epicenter for a single event meaningless. However, the distribution of back azimuth (Figure 4.3 and distance (Figure 4.4) at most stations can provide insight for interpreting the source of events. Only RS05 did not produce enough valid location estimates to be useful in this way. While many cross-correlation picks (1,183) were collected at RS05, only 41 were used to estimate locations and few of these returned valid results. RS07 shows a subtle peak in back azimuths directed towards the south, away from the ice front and distances are concentrated in the near field, implying that located seismicity is mostly distributed and highly local. At RS08 three distinct peaks in back azimuth and distance imply that seismicity is spatially clustered. The two clusters are well aligned with streakline surface features visible in satellite imagery. The third cluster is aligned with rump-like features on the flank of Roosevelt Island. At RS09 a majority of seismicity is clustered

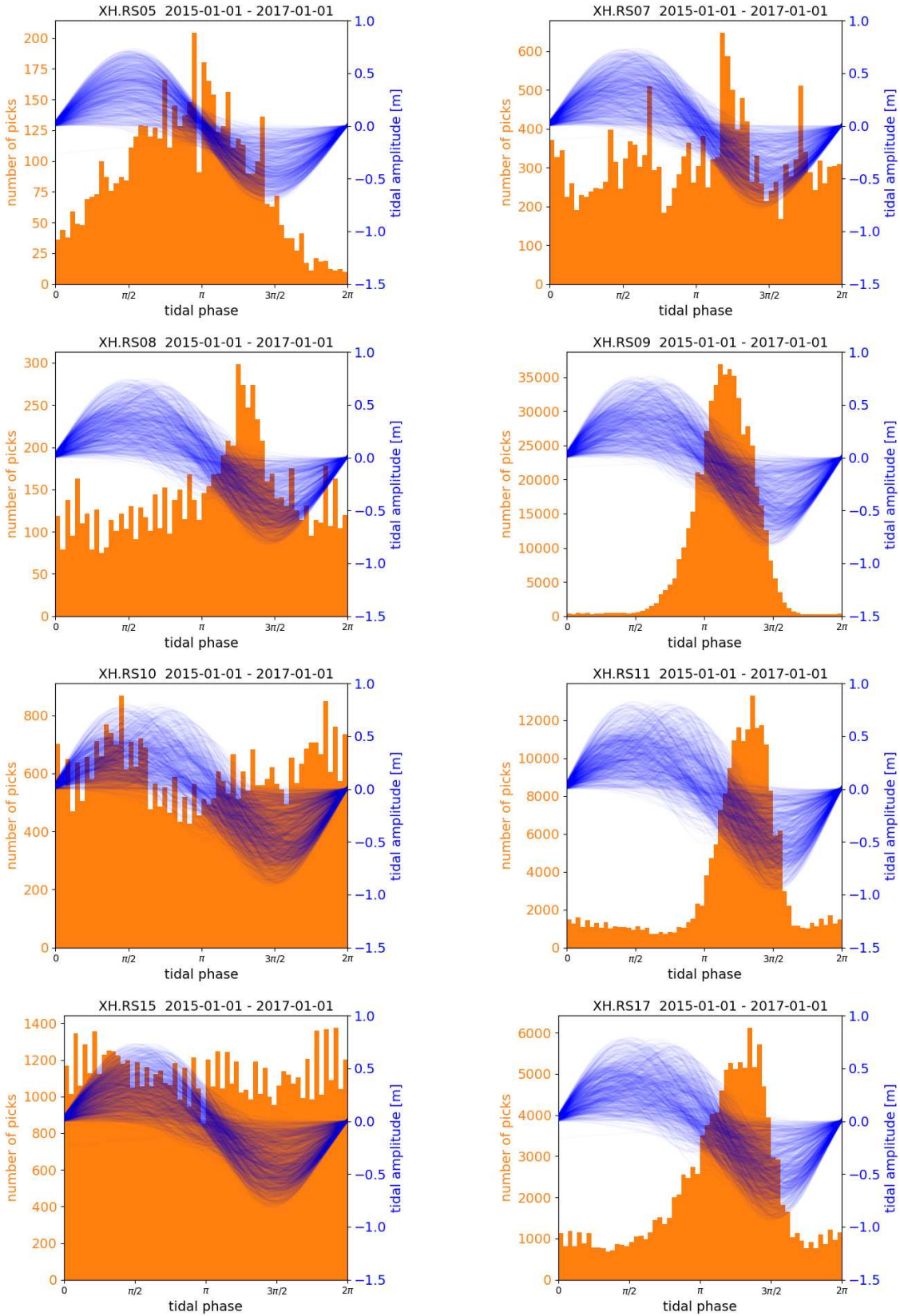


**Figure 4.1:** Cross-correlation picks relative to timing in the tidal cycle.

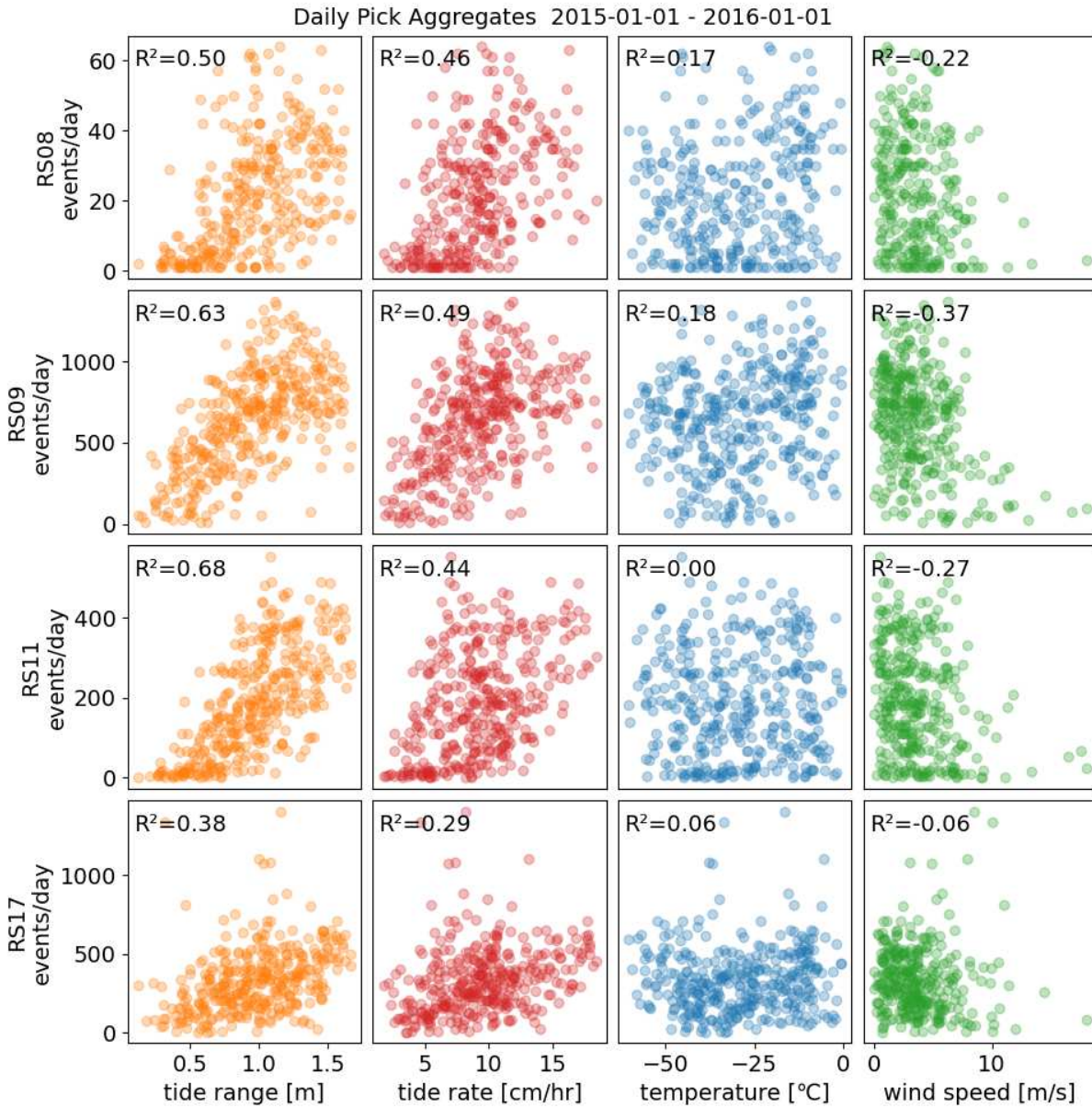


**Figure 4.2:** Scatter plots showing correlation of tidal range, tidal rate of change, air temperature, and wind speed at stations of interest. R-squared values for linear regressions of each plot are shown.

towards the channel between Roosevelt Island and Marie Byrd Land on a topographic rise where surface crevasse are visible in high-resolution satellite imagery (Figure 2.5). A smaller cluster of seismicity branches off the main group that also aligns with surface features. At RS10 seismicity is radially dispersed and broadly distributed in the near field, implying that seismicity detected at this station is not associated with distinct features like small rifts, crevasses, or strand cracks. At RS11, two distinct populations of seismicity that are both aligned with the sides of the ice stream outlet the station is roughly centered in. Interestingly, more seismicity is detected from the northern side at a greater distance which could mean that brittle failure is more common on one side of the ice stream channel. RS15 shows radially distributed seismicity with two peaks roughly east and west of the station. This station is located near mapped shear zones, but seismicity is too local to be from any large surface feature apparent in satellite imagery. RS17 shows bimodal back azimuths and distances with events that cluster near dramatic shear-to-transverse surface crevasses on the leeward side of the Steershead Ice Rise. Ice melange is visible in these large open crevasses which may partially explain the harmonic tremors observed at this station. It is important to note here that the bimodal distance peaks are at  $\sim 2$  and  $\sim 5$  km. The peak in distance at  $\sim 7$  km is a data artifact from bunching of dispersion range estimates caused by the extremely high rate of events causing spectral overlap which interferes with the trace fitting part of the method. A similar effect is also present in the RS11 distance histogram  $\sim 7$  km. This effect can only be removed by determining if multiple events are present in an observation window, and if so skipping the dispersion ranging method.

The coincidence of estimated epicenters with surface features does not necessarily mean that events are sourced from the surface. On ice shelves, particularly near the grounding line, it has been observed that surface features will often form in response to basal channels or crevasses (Daniel et al., 2012). Similarly, the Steershead Crevasses at RS17 have morphology like a small rift and may penetrate deep into the shelf or through it entirely in places, allowing events coincident with their surface expression to happen at any depth. Only constraining the epicenter and not hypocenter was an important limitation of the location scheme in this study. The epicenter estimates are also

limited by the accuracy of the time arrival difference and the dispersion ranging as discussed in section 2.2.

## 4.4 Event Populations

The four event types are broad generalizations about seismicity at the grounded margins. Most clusters detected by REDPy are actually differentiated families within the type A or type B population. This is likely because they come from more distinct sources (surface or basal crevasses) while type C events are likely from spatially distributed sources (within the firn). The detection scheme is biased towards finding more repeatable seismicity like type A and B, but the results reflect the true relative amounts of each type. Many of the templates that were discarded for low signal to noise from few members were very similar to another template, so their members would just group in with the valid template. This is to say that so long as one valid template exists for an event type, that type will be captured by the cross-correlation detection. The interpretations of source mechanisms are intended to guide future studies either using the RIS/DRIS dataset or with new data. The evidence for type A events being sourced from a near-surface crevasse or strand crack is strong. Additional work needs to be done to conclusively prove this interpretation of the source mechanism, but it is a solid hypothesis to work with. Similarly, the evidence for type B events having a basal-crevasse or deep strand crack source is also compelling, especially when compared as a distinct population from type A. Determining the source depth would help support or refute this interpretation, but was not attempted in this work. Other studies have done this in glacial environments using a single station by estimating the angle of incidence from polarization analysis in addition to the back azimuth (Helmstetter et al., 2015). Type C and type D events have less certainty in their interpreted source mechanisms. Type C events are likely sourced in the near-surface firn and represent a spatially distributed phenomenon. However, this work simply has not examined them in enough detail to provide much more information. More could be learned about them by looking at environmental trends leading up to their swarms and by modelling the propagation of thermal perturbations to depth to estimate their source depth. Type D events are

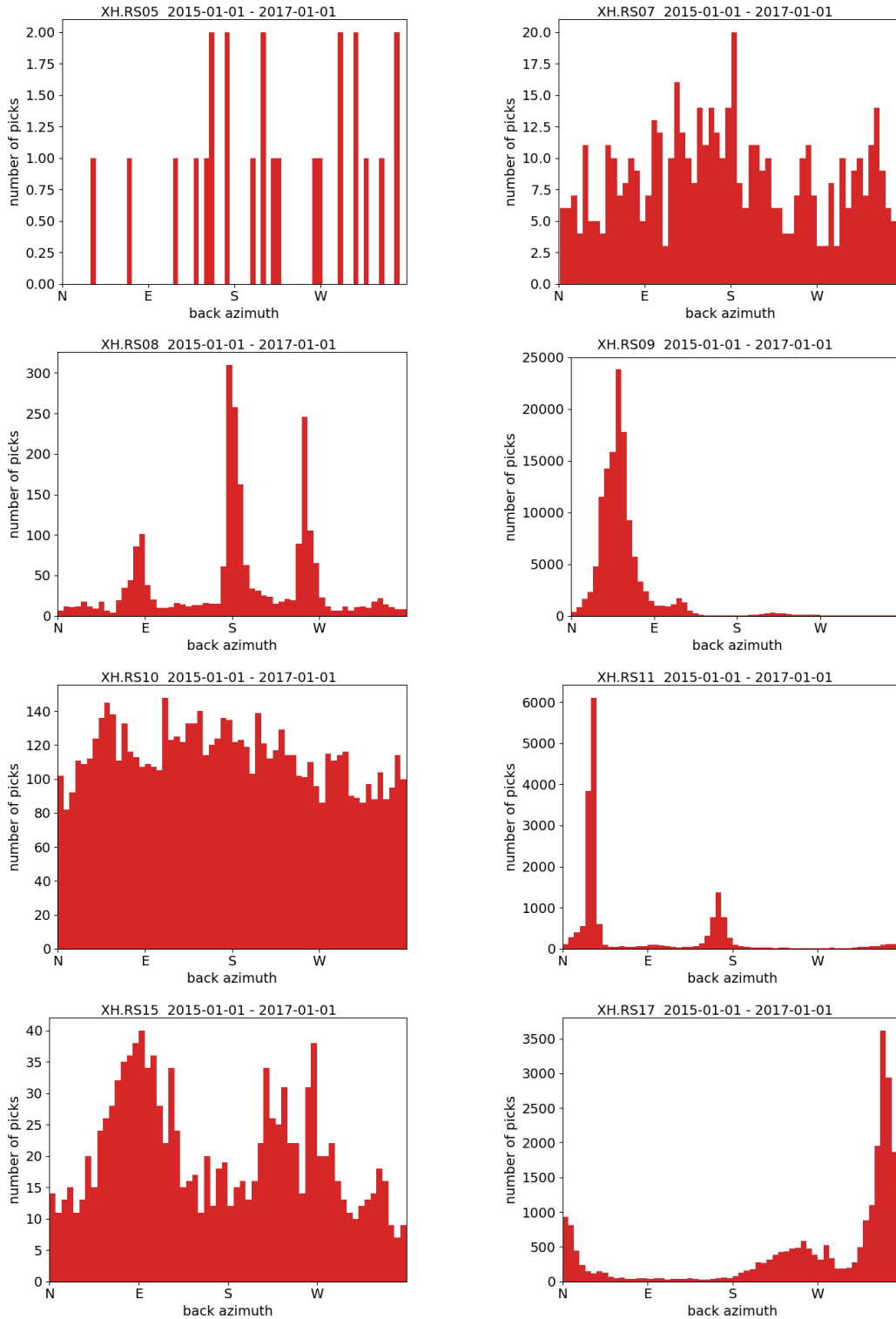


**Figure 4.3:** Histograms of back azimuth for located events. Events with erroneous negative arrival time difference were removed because they are more prone to poor automatic surface wave window selection and thus poor polarization analysis results.

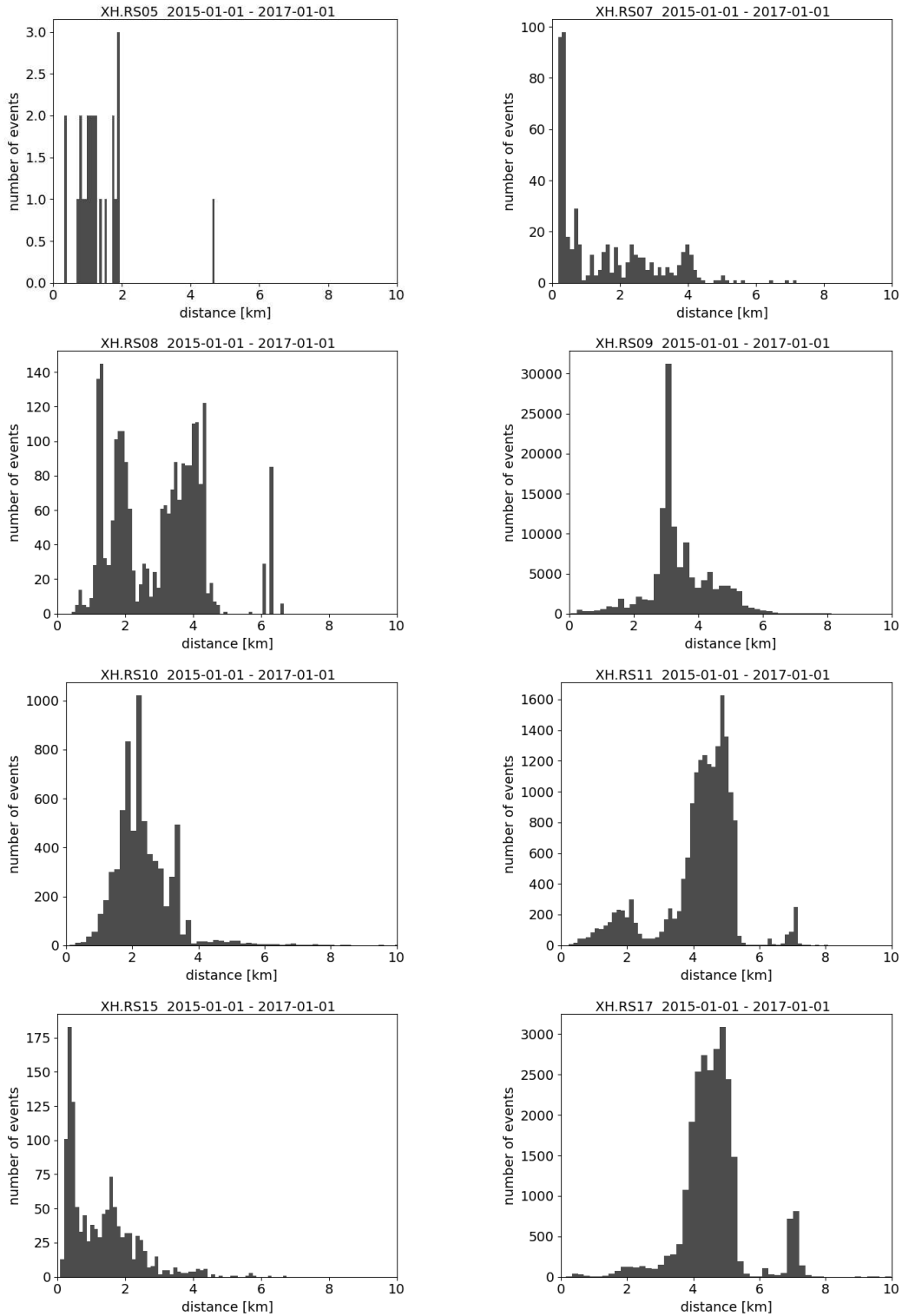


**Figure 4.4:** Histograms of the source-receiver distance averaged between the arrival time difference dispersion ranging methods. Events with bad phase arrival time picks were not assigned a distance and therefore not included here. The effect from bunching of errant dispersion ranges can be seen in small picks at the maximum distance of the distribution in some stations (RS08, RS11, RS17)

very unique signals and their harmonic that do not give many hints to their source depth, making it difficult to interpret a source mechanism. They appear to be phenomenon localized (within the seismic network coverage) to the Steershead Ice Rise, but the diversity of processes occurring around the ice rise does not narrow down possible source mechanisms. Examining seismic studies and data from other ice rises may hold a clue to pursuing the cause of these events however.

## **4.5 Future Directions**

This research serves as a preliminary description of seismic phenomenon observed at the grounded margins of the Ross Ice Shelf. More work needs to be done to conclusively demonstrate source mechanisms for each event type and determine their utility for monitoring dynamic processes within the ice shelf. The first avenue to peruse following this work is simply a rerun of the processing scheme at all stations in full resolution. Lower similarity thresholds, three component template matching, finer dispersion ranging, and location estimate on all picks would produce a much larger result data set to analyze. With the parameters described in this work, processing all data at selected stations takes roughly one week. However, at full resolution this could take a month or more. There are some places where clever programming could improve the efficiency of the processing, but deployment of the code on a faster computer would also be beneficial. A full resolution run would not change the interpretations and conclusion from this work but would provide a stronger foundation for further research. Another improvement would be to implement a formalized classification scheme similar to the Gaussian Mixture Model tested in this work. Accurate classification of events will allow for better differentiation of the tidal and environmental forcing correlated to each type and will also specific seismic data processing methods to be applied only when applicable. For instance, in this work both ranging techniques were designed for type A and type B events. With classification, parameters could be selected for each type of event, including dispersion ranging bandwidth that extends into higher frequencies. Similar to classification, a robust hierarchical clustering analysis would benefit interpreting these events by quantifying the uniqueness of each cluster. Based on the suggested interpretations in this work it

would be expected that type A and type B events would cluster with more dissimilarity (clusters are more different from each other but members are very similar) than type C or type D events that would be more distributed (clusters are more similar to each other, but more variation among members). The dispersion ranging method also warrants additional attention. In this work, the method is limited by the assumption of a crude velocity model and source depth. An Monte-Carlo like inverse method could be used to solve for the velocity model, source characteristics, and range. This would come at vast computational expense, so other improvements could be made without formalizing it as an inverse problem. For instance, the firm model was taken from the RIS interior, but studies have shown that it vary appreciably within and around the ice shelf. This would justify that a new firm model should be developed for each station. Enhancing single station location methods has broad applicability in glacial seismology where deployments are often sparse, but could also greatly benefit planetary seismology as studies will often be limited to a single station. Another way to improve outcomes for this research would be to robustly model various source mechanisms and test them against observations. This was attempted in this work using the OASES software, but proved to be difficult because of the lack of a ground truth velocity model, complexity of implementation, and the compute time to run tests. Of course the best way to illuminate the source mechanisms described in this work would be to deploy a focused study of short-period, nodal, or fiber optic sensors at the grounded margin. Since we have observed that many of the interesting seismic phenomenon occur year-round, a short-term deployment would collect sufficient data to study event types A, B, and D in great detail. However, a long-term or permanent station would need to be deployed to examine why type C seismicity occurred in such greater numbers during the second winter.

## **4.6 November 26 2014 Bolide Explosion**

In a short aside from this work I briefly explored the seismic signature of a bolide explosion that occurred on November 26 2014, just as the RIS/DRIS network began recording data. This was inspired by a similar observation a bolide from two seismic stations in Greenland (Schmerr et al.,

2018). At 2014-11-26T23:16:51 UTC a 0.35 kton bolide exploded at an altitude of 23 km over the Ross Sea at 69.5°S, 179.7°W. Knowing the time and location of the event (retrieved from the NASA CNEOS fireball and bolide data page at [cneos.jpl.nasa.gov/fireballs](http://cneos.jpl.nasa.gov/fireballs)) I was able to plot the data in a seismic record section to identify the subtle waveforms associated with the bolide airblast. The signal is recognizable even 1350 km away from its source on the ice shelf interior at RS18, the farthest station from the ice front. However it was not seen in seismic data from Victoria Land at stations much closer to the source. In part this was because of acoustic shadows in Victoria Land obscuring the airblast in that area. However, the flat geometry and unique wavefield of the RIS allowed this atmospheric event to couple much better with the ice and travel further through the ice than would be possible if it were a grounded glacier. This is supported by the fact that the signal is more apparent in the north-oriented horizontal channel that is roughly perpendicular to the ice front. This event is mostly a curiosity, but these rare occurrences are important terrestrial analogs for planetary seismology because meteor impacts and bolide explosions represent a significant portion of seismogenic activity on other planets. This case from the RIS is a particularly relevant because ice shelves are analogs for the lithosphere of icy satellites.

## **4.7 Summary and Conclusions**

Seismicity at the grounded margins of the Ross Ice Shelf is induced and enhanced by tidal flexure. Tides cause alternating compression and extension at the surface and base of the shelf, cause vertical movement of the floating portion of the margin relative to grounded ice, and at times can reduce the basal drag or allow the infiltration of water further up the grounded surface than usual. These all change the stress field within the ice which is often accommodated by brittle failure or motion between surfaces and can result in a variety of seismic activity. The tides also influence seismicity in the ice shelf interior, but to a much lesser extent with the exception of icequakes sourced from open rifts. The icequakes observed at stations near the grounded margin represent a vast majority of the repeating seismicity recorded by the RIS/DRIS array. This work developed and implemented a detection scheme to identify, cluster, and locate repeating icequakes associated

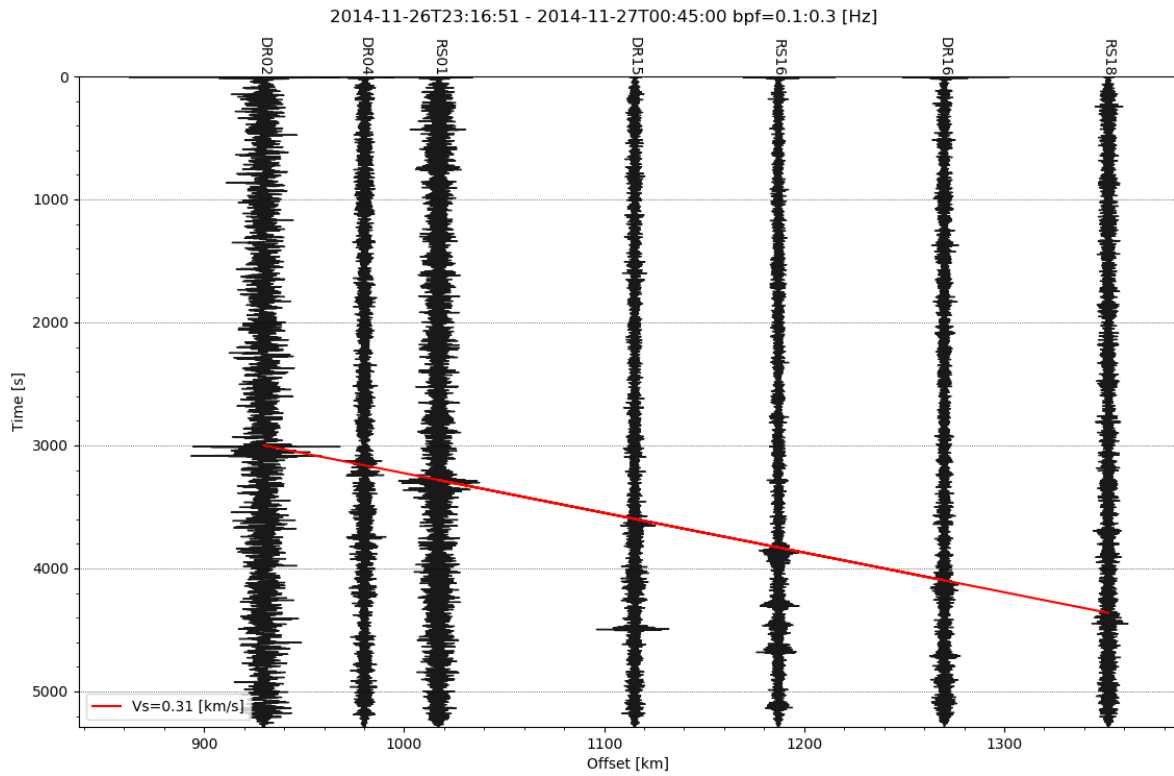


**Figure 4.5:** Record section of data from RIS/DRIS showing the arrival of coupled energy from the bolide airblast. The red line denotes the predicted arrival based on the speed of sound in cold air.

with swarm seismicity. This was done in two passes of the seismic data, first to identify spikes in seismic energy and cluster them based on waveform similarity, then again to use those clusters as templates in a cross-correlation detector to identify smaller amplitude icequakes. Icequake epicenters were estimated for cross-correlation picks with sufficiently large cross-correlation coefficients and signal-to-noise ratios. This produced a catalog of over 940,000 picks with over 342,000 of them considered high quality and used for location estimates. The catalog was examined to describe the four types of events that broadly cover all repeating seismicity observed at grounded margins. Source mechanisms for each event type are suggested but not conclusively proven in this work. Type A events are icequakes sourced from near-surface crevasses or strand cracks that are activated by increased tensile stress from tidal flexure. They occur daily during falling tides and at all times of year with no clear correlation with air temperature. Type B events are icequakes that have an englacial or basal source. They occur only during high tides when the tidal range is sufficiently large. Type C events are likely sourced from a spatially distributed process in the firn. They only occur during periods of prolonged cold and are observed at mid-shelf stations in addition to those near the grounding line. For an unknown reason, these events only occur during the second winter of the RIS/DRIS deployment. Type D events are harmonic tremors that mainly occur near the Steershead Ice Rise. Their source mechanism could be shear failure or basal sliding that results in many small events concluding with a large impulse. They could also be explained by propagation of fluid filled crevasse. The four event types demonstrate the diversity and persistence of seismicity at the grounded margins. In future work, the source mechanisms for these events will be conclusively determined, and their hypocenters will be constrained. This will provide insight into the structure of deforming glacial masses at the grounded margins of the Ross Ice Shelf and could serve as a method to continuously monitor them as they evolve and respond to climate change.

## Chapter 5

# Swarmpy: Automatic Analysis of Swarm Seismicity

Swarmpy is the name I gave to the package of Python software used to process all of the seismic, tidal, and weather data used in this project. Nearly all processing and plotting presented in this thesis was done within Swarmpy, with the exception of running TMD (a MATLAB toolbox) to produce tidal time series, running OASES (a Fortran library) to model dispersion curves, and a MATLAB script that reads OASES output (a function provided by coauthor Julien Chaput) and extracts the group velocity dispersion relationship. While Swarmpy is optimized for working with data from the RIS/DRIS deployment, thought and effort was put into making it extensible to other data sets where repeating seismicity is observed and single-station processing is appropriate, particularly in glacial environments. It was developed based on code from an earlier Python package called SurfCSU I wrote that provided a command line tool to wrap much much of the Obspy functionality to mimic the SAC software tool widely used by seismologists. At the time of writing Swarmpy is  $\sim 4,700$  lines of code and comments. When the manuscript within this thesis is submitted for publication, Swarmpy will be made publicly available as a static git repository allowing others to reproduce the catalog and figures from this project. Then much of the software will be ported back to SurfCSU where development of new processing tools will continue.

### 5.1 Preparing the Swarmpy Environment

Swarmpy can be run on any operating system, but a UNIX based system (Linux or Mac) is recommended. Swarmpy extends many other python packages so using a package manager like Anaconda is highly recommended. The following steps to setup an environment to run Swarmpy will assume the use of Ubuntu Linux operating system and the Anaconda package manager. Depending on how Swarmpy is configured in the following section you may need administrator privileges. I was able to run it through SSH on a university computer that I do not administrator privilege on, but found it easier to debug and run on my local machine with this ability.

Swarmpy has three main dependencies:

- Python 3.7+, the main scripting language that all dependencies are written in.
- Anaconda, a software package manager that handles creating and using environments.
- REDPy, a seismology tool written in python that must be run as a subprocess.

The details of installing and configuring these will not be covered in detail here as there are comprehensive guides available online. Anaconda can handle the installation of Python 3.7 which saves a step. It has exhaustive documentation for installation and use. While Anaconda does have paid products, the free "individual edition" does everything needed to run Swarmpy. I recommend getting acquainted with Anaconda after installing before moving on to install REDPy. An excellent resource for this is following along with their test drive or getting started page ([bit.ly/tryconda](http://bit.ly/tryconda)). It is best to create an Anaconda environment exclusively for the purpose of running Swarmpy. This can be done by manually creating a named environment, then adding packages as needed or it can be done by importing an environment from a yml file. The file `swarmsnek.yml` can be used to import an environment to run Swarmpy and is included with the Swarmpy git distribution. To my knowledge the newer versions of all required packages should have backwards compatibility with running Swarmpy, with the exception of NumPy which must be version 1.15.4 to run REDPy.

REDPy (Repeating Earthquake Detector in Python) is a earthquake detection tool used by Swarmpy to find initial event families that are used to build templates (Hotovec-Ellis and Jeffries, 2016). REDPy is essentially a wrapper for implementing the Obspy STA/LTA detector and Python hierarchical clustering. It also produces high-quality interactive information products that are useful in diagnosing issues with Swarmpy configuration, determining the best parameters to use, and inspecting intermediate information products about repeating seismicity in the data set. The REDPy results are great final products in their own right as well. REDPy cannot be installed with Anaconda as it is not an extensible package. I recommend following all the REDPy documentation and testing it on the configuration included in its distribution. REDPy does not need

to be added to the user's path but you will need to add the installation directory to the Swarmpy configuration file so that it can be run through subprocesses as described in the following section.

## 5.2 Configuring Swarmpy

Swarmpy is controlled through a configuration and a parameter file. The configuration file contains settings that are exclusive to the machine Swarmpy is running on and shouldn't need to be changed once set except in special circumstances. The parameter file contains settings that define a single run of the main Swarmpy script. A default.config and default.param file are included in the distribution that are well-commented to explain each definition when they are not obvious. Both files should be read in their entirety to become familiar with what options are available. In both files, lines beginning with a "#" are commented out, all assignments require no spaces between the variable and its value, and blank lines can be used to separate sections.

The configuration file contains the following settings:

- data\_dir - This is where seismic and weather data are downloaded to. It stores result tables.
- figs\_dir - Any PNG figure that is produced will be exported to this directory.
- redout\_dir - The results of the REDPy runs will be exported to this directory.
- redexe\_dir - This defined where you have REDPy installed on your machine.
- iris\_user - If using a restricted dataset an IRIS user and password must be provided.
- iris\_auth - Be careful not to upload your config file somewhere with this field filled out.

The parameters file contains the following settings:

- t1 - Start time. Best to set this before data begins if processing an entire data set.
- t2 - End time. Best to set this after data end if processing an entire data set.
- dnslc - Dynamic NSLC seed code. Allows user to include one or more stations/channels.

- `main_channel` - The channel used when only one is needed (for processing and figures).
- `bodyfmin` - The frequency (Hz) that defines the lower end of the upper band.
- `bodyfmax` - The frequency (Hz) that defines the upper end of the upper band.
- `surffmin` - The frequency (Hz) that defines the lower end of the lower band.
- `surffmax` - The frequency (Hz) that defines the upper end of the lower band.
- `red_minorph` - Minimum number of days before a repeating event can be added to a cluster.
- `red_maxorph` - Maximum number of days before an unclustered event becomes an orphan.
- `red_nsec` - Number of seconds of seismic data to processes at once (depends on memory).
- `red_lwin` - LTA window length in seconds.
- `red_swin` - STA window length in seconds.
- `red_trigon` - STA/LTA trigger on threshold.
- `red_trigoff` - STA/LTA trigger off threshold.
- `red_winlen` - REDPy cross-correlation window length in samples (2 $\hat{n}$  is best).
- `red_cmin` - REDPy cross-correlation coefficient minimum to be clustered.
- `red_minplot` - Minimum number of cluster members to appear on the REDPy timeline plot.
- `red_dybin` - Width (in days) of bins for the REDPy histogram subplot.
- `red_hrbin` - Width (in hours) of bin for the REDPy "recent" histogram subplot.
- `red_occurbin` - Width (in hours) of bars in the REDPy occurrence plot.
- `red_recbin` - Width (in hours) of bars in the REDPy "recent" occurrence plot.
- `red_recplot` - Number of days prior to show on the "recent" timeline.

- red\_kurtfmax - See Kurtosis parameters in REDPy documentation.
- red\_oratiomax - See Kurtosis parameters in REDPy documentation.
- red\_telefi - See teleseism filtering in REDPy documentation.
- red\_teleok - See teleseism filtering in REDPy documentation.
- swarm\_wind - Defines window (in seconds) to cluster and differentiate swarms.
- swarm\_nmin - Minimum number of events for time-clustered triggers/picks to be a swarm.
- template\_pre - Time (in seconds) before a trigger to extend event observation window.
- template\_post - Time (in seconds) after a trigger to extend event observation window.
- template\_buffer - Buffer (in seconds). Ideally set to 10% of template\_pre+template\_post.
- correlation\_minsim - Minimum similarity value for cross-correlation picks.
- correlation\_trigdist - Minimum distance (in seconds) between cross-correlation picks.
- location\_Vp - Assumed P-wave velocity used in arrival time differencing.
- location\_Vr - Assumed Rayleigh wave velocity used in arrival time differencing.
- wxstn - Three letter code to define the AWS weather station to use.
- scroll\_wind - Length of scroll plot window (in days)
- scroll\_step - Step between scroll plots (in days)
- scroll\_vmin - Optional. Minimum value to saturate the spectrogram in scroll plots.
- scroll\_vmax - Optional. Maximum value to saturate the spectrogram in scroll plots.
- flag\_make\_event\_plots - "True" or "False" to make (compute-expensive) event plots.

## 5.3 Running Swarmpy

Swarmpy is simply run through the terminal by calling Python with the `swarm.py` script. This script will first parse the configuration and parameter files, then start the main method of the program. The console will print out lots of logging information that will provide a status of where in the processing steps Swarmpy is and assure you that it is still running. For a multi-year dataset Swarmpy will take days to run just for a single station. If it is your first time running Swarmpy and seismic data needs to be downloaded. This will take even longer. It is recommended that you use a terminal multiplexer like Tmux to run Swarmpy so that you can close and return to the terminal window where it is running. This will also allow you to run instances of Swarmpy for different stations at the same time. Never run Swarmpy on the same station at the same time because this can produce unexpected results. To run multiple instances of swarmpy, simply change the `dnslc` value before starting Swarmpy each time. The configuration is held in memory, so these files can be edited without affecting an instance of Swarmpy that is already running. Be careful when running multiple instances of Swarmpy that you do not accidentally run out of RAM or disk space. Use tools like `htop` to monitor your RAM usage and `baobab` to monitor your disk usage while getting a feel for how much resources Swarmpy will consume on your machine. Swarmpy will produce various errors if it runs into a shortage of RAM or disk. Usually this will be a helpful `OutOfMemoryError`, saying what caused it. However, sometimes you will only see "Killed" as the last logged entry to the console which means you have run out of RAM mid-process. In this case you will need to restart Swarmpy and try again either with more resources allocated, or with fewer instances of Swarmpy running. To restart at a particular processing step, edit the main method `"go()"` at the top of the `swarm.py` script to comment out steps that have already been successfully completed. This tactic is also useful when diagnosing issues, changing parameters, and debugging as you are unlikely to want to run the whole processing scheme over again. It can be helpful to start Swarmpy by running each of these steps one at a time and inspecting the intermediate results. If following the chain of python methods to see what is happening is too difficult for you, then

it will be hard to fix any problems that may arise in later processing steps. To use this software effectively it is critical to become familiar with the various scripts called by the main method.

## 5.4 Examining Swarmpy Results

Swarmpy exports all results to the directories defined in the configuration file. After downloading the weather and seismic data, the first step Swarmpy does is extend the REDPy program. The results from REDPy are stored separately from data or figure outputs. It is useful to inspect the html files that display plots showing timelines of swarm seismicity and information pages about each cluster which REDPy generates. The user defined data directory will store flat files, CSV files, and pickle files that contain data structures of cluster templates, cross-correlation picks, swarm aggregates, and event catalogs. The flat files and CSV files are human readable and can be viewed or edited in any text editor or excel. These can also be used as input for analysis or plotting in Matlab or other programming languages. Pickle files are exported serialized versions of Python data structures held in memory. These mostly contain intermediate information that needs to be stored on disk for Swarmpy but are unlikely to be of interest to the user because a better data product will be derived from them in a following processing step. All figures produced by Swarmpy will be exported to the `figs_dir` defined in the configuration file. By default, these will include plots of cluster templates, scroll plots, swarm plots, and event plots. There are also other plotting scripts included in the distribution that made the figures in this thesis. These can be called by uncommenting their methods within the main method, but this should not be done until you have confirmed that Swarmpy processing has been successful because they mostly rely on the final pick and event catalogs.

# Bibliography

- Anandakrishnan, S. and Alley, R. B. (1997). Tidal forcing of basal seismicity of ice stream c, west antarctica, observed far inland. *Journal of Geophysical Research: Solid Earth*, 102(B7):15183–15196.
- Anderson, J. B., Shipp, S. S., Lowe, A. L., Wellner, J. S., and Mosola, A. B. (2002). The antarctic ice sheet during the last glacial maximum and its subsequent retreat history: a review. *Quaternary Science Reviews*, 21(1-3):49–70.
- Anthony, R. E., Aster, R. C., Wiens, D., Nyblade, A., Anandakrishnan, S., Huerta, A., Winberry, J. P., Wilson, T., and Rowe, C. (2014). The Seismic Noise Environment of Antarctica. *Seismological Research Letters*, 86(1):89–100.
- Aster, R. and Winberry, J. P. (2017). Glacial seismology. *Reports On Progress in Physics*, 80.
- Aster, R. C., Shearer, P. M., and Berger, J. (1990). Quantitative measurements of shear wave polarizations at the anza seismic network, southern california: Implications for shear wave splitting and earthquake prediction. *Journal of Geophysical Research: Solid Earth*, 95(B8):12449–12473.
- Baker, M. G., Aster, R. C., Anthony, R. E., Chaput, J., Wiens, D. A., Nyblade, A., Bromirski, P. D., Gerstoft, P., and Stephen, R. A. (2019). Seasonal and spatial variations in the ocean-coupled ambient wavefield of the ross ice shelf. *Journal of Glaciology*, 65(254):912–925.
- Barruol, G., Cordier, E., Bascou, J., Fontaine, F. R., Legrésy, B., and Lescarmontier, L. (2013). Tide-induced microseismicity in the mertz glacier grounding area, east antarctica. *Geophysical Research Letters*, 40(20):5412–5416.
- Bassis, J. N., Fricker, H. A., Coleman, R., Bock, Y., Behrens, J., Darnell, D., Okal, M., and Minster, J.-B. (2007). Seismicity and deformation associated with ice-shelf rift propagation. *Journal of Glaciology*, 53(183):523–536.

- Benn, D. and Evans, D. J. (2014). *Glaciers and glaciation*. Routledge.
- Bromirski, P. D., Diez, A., Gerstoft, P., Stephen, R. A., Bolmer, T., Wiens, D., Aster, R., and Nyblade, A. (2015). Ross ice shelf vibrations. *Geophysical Research Letters*, 42(18):7589–7597.
- Bromirski, P. D. and Stephen, R. A. (2012). Response of the ross ice shelf, antarctica, to ocean gravity-wave forcing. *Annals of Glaciology*, 53(60).
- Chaput, J., Aster, R. C., McGrath, D., Baker, M., Anthony, R. E., Gerstoft, P., Bromirski, P., Nyblade, A., Stephen, R. A., Wiens, D. A., et al. (2018). Near-surface environmentally forced changes in the ross ice shelf observed with ambient seismic noise. *Geophysical Research Letters*, 45(20):11–187.
- Chen, Z., Bromirski, P., Gerstoft, P., Stephen, R., Lee, W. S., Yun, S., Olinger, S., Aster, R., Wiens, D., and Nyblade, A. A. (2019). Ross ice shelf icequakes associated with ocean gravity wave activity. *Geophysical Research Letters*, 46(15):8893–8902.
- Chen, Z., Bromirski, P. D., Gerstoft, P., Stephen, R. A., Wiens, D. A., Aster, R. C., and Nyblade, A. A. (2018). Ocean-excited plate waves in the ross and pine island glacier ice shelves. *Journal of Glaciology*, 64(247):730–744.
- Colgan, W., Rajaram, H., Abdalati, W., McCutchan, C., Mottram, R., Moussavi, M. S., and Grigsby, S. (2016). Glacier crevasses: Observations, models, and mass balance implications. *Reviews of Geophysics*, 54(1):119–161.
- Cristini, L., Grosfeld, K., Butzin, M., and Lohmann, G. (2012). Influence of the opening of the drake passage on the cenozoic antarctic ice sheet: a modeling approach. *Palaeogeography, Palaeoclimatology, Palaeoecology*, 339:66–73.
- Cunningham, W. D., Dalziel, I. W., Lee, T.-Y., and Lawver, L. A. (1995). Southernmost south america-antarctic peninsula relative plate motions since 84 ma: Implications for the tec-

- tonic evolution of the scotia arc region. *Journal of Geophysical Research: Solid Earth*, 100(B5):8257–8266.
- Daniel, M., Steffen, K., Scambos, T., Rajaram, H., Casassa, G., and Lagos, J. L. R. (2012). Basal crevasses and associated surface crevassing on the larsen c ice shelf, antarctica, and their role in ice-shelf instability. *Annals of glaciology*, 53(60):10–18.
- DeConto, R. M. and Pollard, D. (2016). Contribution of antarctica to past and future sea-level rise. *Nature*, 531(7596):591–597.
- Diez, A., Bromirski, P. D., Gerstoft, P., Stephen, R. A., Anthony, R. E., Aster, R. C., Cai, C., Nyblade, A., and Wiens, D. A. (2016). Ice shelf structure derived from dispersion curve analysis of ambient seismic noise, ross ice shelf, antarctica. *Geophysical Journal International*, 205(2):785–795.
- Du Toit, A. L. (1937). Our wandering continents: an hypothesis of continental drifting.
- Fretwell, P., Pritchard, H. D., Vaughan, D. G., Bamber, J. L., Barrand, N. E., Bell, R., Bianchi, C., Bingham, R., Blankenship, D. D., Casassa, G., et al. (2013). Bedmap2: improved ice bed, surface and thickness datasets for antarctica. *The Cryosphere*, 7(1):375–393.
- Fricker, H. A. and Padman, L. (2006). Ice shelf grounding zone structure from icesat laser altimetry. *Geophysical Research Letters*, 33(15).
- Furst, J., Durand, G., Gillet-Chaulet, G., Tavaré, L., Rankl, M., Braun, M., and Gagliardini, O. (2016). The safety band of antarctic ice shelves. *Nature Climate Change*.
- Hammer, C., Ohrnberger, M., and Schlindwein, V. (2015). Pattern of cryospheric seismic events observed at ekström ice shelf, antarctica. *Geophysical Research Letters*, 42(10):3936–3943.
- Hanks, T. C. and Kanamori, H. (1979). A moment magnitude scale. *Journal of Geophysical Research: Solid Earth*, 84(B5):2348–2350.

- Hauer, M. E. (2017). Migration induced by sea-level rise could reshape the us population landscape. *Nature Climate Change*, 7(5):321–325.
- Heeszel, D. S., Fricker, H. A., Bassis, J. N., O’Neel, S., and Walter, F. (2014). Seismicity within a propagating ice shelf rift: the relationship between icequake locations and ice shelf structure. *Journal of Geophysical Research: Earth Surface*, 119(4):731–744.
- Helmstetter, A., Moreau, L., Nicolas, B., Comon, P., and Gay, M. (2015). Intermediate-depth icequakes and harmonic tremor in an alpine glacier (glacier d’argentière, france): Evidence for hydraulic fracturing? *Journal of Geophysical Research: Earth Surface*, 120(3):402–416.
- Hotovec-Ellis, A. and Jeffries, C. (2016). Near real-time detection, clustering, and analysis of repeating earthquakes: Application to mount st. helens and redoubt volcanoes. In *Seismological Society of America Annual Meeting*.
- Hulbe, C. L., Klinger, M., Masterson, M., Catania, G., Cruikshank, K., and Bugni, A. (2016). Tidal bending and strand cracks at the kamb ice stream grounding line, west antarctica. *Journal of Glaciology*, 62(235):816–824.
- Krischer, L., Megies, T., Barsch, R., Beyreuther, M., Lecocq, T., Caudron, C., and Wassermann, J. (2015). ObsPy: a bridge for seismology into the scientific python ecosystem. *Computational Science & Discovery*, 8(1):014003.
- Lazzara, M. A., Weidner, G. A., Keller, L. M., Thom, J. E., and Cassano, J. J. (2012). Antarctic automatic weather station program: 30 years of polar observation. *Bulletin of the American Meteorological Society*, 93(10):1519–1537.
- LeDoux, C. M., Hulbe, C. L., Forbes, M. P., Scambos, T. A., and Alley, K. (2017). Structural provinces of the ross ice shelf, antarctica. *Annals of Glaciology*, 58(75pt1):88–98.
- Livermore, R., Nankivell, A., Eagles, G., and Morris, P. (2005). Paleogene opening of drake passage. *Earth and Planetary Science Letters*, 236(1-2):459–470.

- Lombardi, D., Benoit, L., Camelbeeck, T., Martin, O., Meynard, C., and Thom, C. (2016). Bimodal pattern of seismicity detected at the ocean margin of an antarctic ice shelf. *Geophysical Journal International*, 206(2):1375–1381.
- MacAyeal, D. R., Banwell, A. F., Okal, E. A., Lin, J., Willis, I. C., Goodsell, B., and MacDonald, G. J. (2019). Diurnal seismicity cycle linked to subsurface melting on an ice shelf. *Annals of Glaciology*, 60(79):137–157.
- Maldonado, A., Balanyá, J. C., Barnolas, A., Galindo-Zaldívar, J., Hernández, J., Jabaloy, A., Livermore, R., Martínez-Martínez, J. M., Rodríguez-Fernández, J., De Galdeano, C. S., et al. (2000). Tectonics of an extinct ridge-transform intersection, drake passage (antarctica). *Marine Geophysical Researches*, 21(1-2):43–68.
- Martin, S., Drucker, R., Aster, R., Davey, F., Okal, E., Scambos, T., and MacAyeal, D. (2010). Kinematic and seismic analysis of giant tabular iceberg breakup at cape adare, antarctica. *Journal of Geophysical Research: Solid Earth*, 115(B6).
- Mikesell, T., van Wijk, K., Haney, M. M., Bradford, J. H., Marshall, H.-P., and Harper, J. T. (2012). Monitoring glacier surface seismicity in time and space using rayleigh waves. *Journal of Geophysical Research: Earth Surface*, 117(F2).
- Naish, T., Powell, R., Levy, R., Wilson, G., Scherer, R., Talarico, F., Krissek, L., Niessen, F., Pompilio, M., Wilson, T., et al. (2009). Obliquity-paced pliocene west antarctic ice sheet oscillations. *Nature*, 458(7236):322–328.
- Noerdlinger, P. D. and Brower, K. R. (2007). The melting of floating ice raises the ocean level. *Geophysical Journal International*, 170(1):145–150.
- Olinger, S. D., Lipovsky, B. P., Wiens, D. A., Aster, R. C., Bromirski, P. D., Chen, Z., Gerstoft, P., Nyblade, A. A., and Stephen, R. A. (2019). Tidal and thermal stresses drive seismicity along a major ross ice shelf rift. *Geophysical Research Letters*, 46(12):6644–6652.

- Osten-Woldenburg, H. V. D. (1990). Icequakes on Ekström ice shelf near Atka Bay, Antarctica. *Journal of Glaciology*, 36(122):31–36.
- Padman, L. and Erofeeva, S. (2005). Tide model driver (tmd) manual. *Earth and Space Research*.
- Padman, L., Erofeeva, S., and Joughin, I. (2003). Tides of the Ross Sea and Ross Ice Shelf cavity. *Antarctic Science*, 15(1):31–40.
- Padman, L., Fricker, H. A., Coleman, R., Howard, S., and Erofeeva, L. (2002). A new tide model for the Antarctic ice shelves and seas. *Annals of Glaciology*, 34:247–254.
- Padman, L., Siegfried, M. R., and Fricker, H. A. (2018). Ocean tide influences on the Antarctic and Greenland ice sheets. *Reviews of Geophysics*, 56(1):142–184.
- Paolo, F. S., Fricker, H. A., and Padman, L. (2015). Volume loss from Antarctic ice shelves is accelerating. *Science*, 348(6232):327–331.
- Pratt, M. J., Winberry, J. P., Wiens, D. A., Anandakrishnan, S., and Alley, R. B. (2014). Seismic and geodetic evidence for grounding-line control of Whillans ice stream stick-slip events. *Journal of Geophysical Research: Earth Surface*, 119(2):333–348.
- Rignot, E., Casassa, G., Gogineni, P., Krabill, W., Rivera, A., and Thomas, R. (2004). Accelerated ice discharge from the Antarctic Peninsula following the collapse of Larsen B ice shelf. *Geophysical Research Letters*, 31(18).
- Rignot, E., Jacobs, S., Mouginot, J., and Scheuchl, B. (2013). Ice-shelf melting around Antarctica. *Science*, 341(6143):266–270.
- Rignot, E., Padman, L., MacAyeal, D. R., and Schmelz, M. (2000). Observation of ocean tides below the Filchner and Ronne ice shelves, Antarctica, using synthetic aperture radar interferometry: Comparison with tide model predictions. *Journal of Geophysical Research: Oceans*, 105(C8):19615–19630.

- Robel, A. A., Tsai, V. C., Minchew, B., and Simons, M. (2017). Tidal modulation of ice shelf buttressing stresses. *Annals of Glaciology*, 58(74):12–20.
- Scambos, T. A., Bohlander, J., Shuman, C. A., and Skvarca, P. (2004). Glacier acceleration and thinning after ice shelf collapse in the larsen b embayment, antarctica. *Geophysical Research Letters*, 31(18).
- Scambos, T. A., Hulbe, C., Fahnestock, M., and Bohlander, J. (2000). The link between climate warming and break-up of ice shelves in the antarctic peninsula. *Journal of Glaciology*, 46(154):516–530.
- Schmerr, N. C., Bailey, H., DellaGiustina, D., Bray, V. J., Habib, N., Pettit, E. C., Dahl, P., Quinn, T., Marusiak, A. G., Avenson, B., et al. (2018). The 2018 qaanaaq fireball: A seismic recording of a meteorite impact event into the greenland ice sheet. In *AGU Fall Meeting Abstracts*.
- Schmidt, H. (2004). Oases, user guide and reference manual, version 3.1. *Department of Ocean Engineering Massachusetts Institute of Technology*.
- Stein, S. and Wysession, M. (2009). *An introduction to seismology, earthquakes, and earth structure*. John Wiley & Sons.
- Stewart, C. L., Christoffersen, P., Nicholls, K. W., Williams, M. J., and Dowdeswell, J. A. (2019). Basal melting of ross ice shelf from solar heat absorption in an ice-front polynya. *Nature Geoscience*, 12(6):435–440.
- Still, H., Campbell, A., and Hulbe, C. (2019). Mechanical analysis of pinning points in the ross ice shelf, antarctica. *Annals of Glaciology*, 60(78):32–41.
- Tinto, K., Padman, L., Siddoway, C., Springer, S., Fricker, H., Das, I., Tontini, F. C., Porter, D., Frearson, N., Howard, S., et al. (2019). Ross ice shelf response to climate driven by the tectonic imprint on seafloor bathymetry. *Nature Geoscience*, 12(6):441–449.

- van den Broeke, M. (2008). Depth and density of the antarctic firn layer. *Arctic, Antarctic, and Alpine Research*, 40(2):432–438.
- Vidale, J. E. (1986). Complex polarization analysis of particle motion. *Bulletin of the Seismological society of America*, 76(5):1393–1405.
- Walter, F., Roux, P., Roeoesli, C., Lecointre, A., Kilb, D., and Roux, P.-F. (2015a). Using glacier seismicity for phase velocity measurements and green's function retrieval. *Geophysical Journal International*, 201(3):1722–1737.
- Walter, F., Roux, P., Roeoesli, C., Lecointre, A., Kilb, D., and Roux, P.-F. (2015b). Using glacier seismicity for phase velocity measurements and green's function retrieval. *Geophysical Journal International*, 201(3):1722–1737.
- Yokoyama, Y., Anderson, J. B., Yamane, M., Simkins, L. M., Miyairi, Y., Yamazaki, T., Koizumi, M., Suga, H., Kusahara, K., Prothro, L., et al. (2016). Widespread collapse of the ross ice shelf during the late holocene. *Proceedings of the National Academy of Sciences*, 113(9):2354–2359.
- Zachos, J., Pagani, M., Sloan, L., Thomas, E., and Billups, K. (2001). Trends, rhythms, and aberrations in global climate 65 ma to present. *science*, 292(5517):686–693.